UC Davis

UC Davis Electronic Theses and Dissertations

Title

Thermally Tunable Perovskite-Oxide Devices for Infrared, Terahertz, and RF Frequencies

Permalink

https://escholarship.org/uc/item/8gr4r5z2

ISBN

9798193262145

Author

Samarah, Ziyad

Publication Date

2026-09-08

Peer reviewed|Thesis/dissertation

eScholarship.org Powered by the California Digital Library
University of California

Thermally Tunable Perovskite-Oxide Devices for Infrared, Terahertz, and RF Frequencies

By

Ziyad Samarah
THESIS

Submitted in partial satisfaction of the requirements for the degree of

MASTER OF SCIENCE

in

Electrical Engineering

in the

OFFICE OF GRADUATE STUDIES

of the

UNIVERSITY OF CALIFORNIA

DAVIS

Approved:

J. Sebastián Gómez-Díaz, Chair

William Putnam

Yayoi Takamura

Committee in Charge

2026

Abstract

Thermally tunable materials can provide the foundation for reconfigurable electromagnetic devices whose response can be modified without physically changing device geometry. This thesis investigates thermally tunable perovskite-oxide devices based primarily on strontium titanate (STO), a high-permittivity material with investigated temperature-dependent dielectric and optical properties. Electrical biasing of thin-film indium tin oxide (ITO) was used to generate localized Joule heating on STO. This enables controlled changes in material response across the investigated infrared, terahertz, and RF frequency regimes. The thermal platform was first developed and characterized using electrical measurements, thermal imaging, and COMSOL simulations to relate applied bias to sample heating. Terahertz time-domain spectroscopy (THz-TDS) showed a large tunable response in pulse delay and refractive index, demonstrating strong thermal tunability of STO. Fourier Transform Infrared (FTIR) spectroscopy measurements showed weaker but measurable tunable changes in reflectance, with the strongest infrared response in the larger wavelengths of the measured infrared band. To investigate the thermally tunable response of STO at radio frequencies, a coplanar waveguide device was also designed and measured. The high permittivity of STO introduced significant design challenges but enabled a clear, tunable response in transmission in the measured RF band. These results demonstrate that induced heating can modify the electromagnetic response of STO across multiple frequency regimes, providing a foundation for the development of STO-based thermally tunable electromagnetic devices.

Acknowledgements

To start, I would like to express my sincere gratitude to my advisor, Professor Gomez-Diaz, for his continuous support, guidance, and compassion throughout this project. His mentorship has helped me grow both technically and professionally, and I have learned a great deal from his insight and encouragement during my time in the research group. I would also like to thank Ph.D. candidates Damia Casajuana and Scott Bricker, as well as my fellow lab members Praneeth Eravalli and Parssa Alimadad, for their support, advice, and involvement in these projects throughout my masters. Their help and contribution significantly helped with the progression of my masters made this process much more meaning and insightful. Lastly, I would like to thank Professor Putnam and Professor Takamura for taking their time to review and be part of my thesis committee.

Table of Contents

List of Figures vi

1 Introduction 1
1.1 Tunable Electromagnetic Materials 1
1.2 Motivation 2
1.3 Materials Systems 4
1.3.1 Strontium Titanate Material Overview 4
1.3.2 Indium Tin Oxide Material Overview 5
1.4 Research Objectives and Thesis Scope 6
1.4.1 Research Objectives 6
1.4.2 Thesis Scope and Organization 7
2 Development of Thermally Controlled Device Platforms 9
2.1 Introduction & Overview 9
2.2 COMSOL Simulations 10
2.3 Prototype PCB Design and Device Integration 15
2.4 Sample Fabrication 18
2.5 I-V Analysis 19
2.6 Thermal Analysis 21
2.7 Summary 23
3 Thermally Controlled Optical Devices 25
3.1 Introduction & Overview 25
3.2 Thermally Engineered STO: Terahertz Response 25
3.2.1 Section Overview 25
3.2.2 THz-TDs System Overview 26
3.2.3 THz-TDS System Calibration 27
3.2.4 THz-TDS System Characterization 32
3.2.5 Thermally Tunable Response of STO: Terahertz 34
3.3 Thermally Engineered STO: Infrared Response 38
3.3.1 Section Overview 38

3.3.2 Literature Review: Infrared Response of STO 39
3.3.3 Infrared Measurements & Result Analysis 40
3.4 Summary 43
4 Thermally Controlled Guided Device 44
4.1 Introduction & Overview 44
4.2 Coplanar waveguides on STO 44
4.2.1 High-Permittivity Substrate Design Considerations 44
4.2.2 CPW Design Geometry Optimization 46
4.2.3 Finalized Design Simulation Results 49
4.3 Device Fabrication 51
4.4 PCB Prototyping 52
4.4.1 Sample PCB Design Requirements 52
4.4.2 PCB CPW Feedline Design & Simulation 53
4.4.3 Final PCB Layout 56
4.5 Experimental Characterization of Device 57
4.5.1 Experimental Setup 57
4.5.2 Device S-Parameter Measurements 59
4.5.3 Bias-Dependent Tunable Response 63
4.6 Summary 65
5 Conclusions & Future Work 66
5.1 Conclusions 66
5.2 Future Work 67

LIST OF FIGURES

Figure 1.1: a) Crystal structure of cubic $SrTiO_3$ showing the Sr, Ti, and O atomic positions. Reproduced from [7]. b) Relative and imagine permittivity of STO from 10^2 to 10^{14} Hz reproduced from [8]. 4

Figure 2.1: COMSOL 4-layer PCB model geometry for the thermally controlled STO sample platform, (a) the full 3D PCB model, (b) the top view layout with copper vias and central STO sample, & (c) the side view cross section of the copper layers and FR-4 substrate. 10

Figure 2.2: Resulting temperature from COMSOL simulation of ITO/STO via a 30mabias..... 12

Figure 2.3: Simulated STO thermal gradient response for varying PCB copper layer configurations. 13

Figure 2.4: Simulated thermal gradient magnitude across the STO sample for two contact configurations: (a) STO without Cu contacts and (b) STO with Cu contacts. The results illustrate the effect of Cu contacts on the spatial thermal-gradient distribution across the sample. 14

Figure 2.5: a) Device set-up in 3D printed PCB holder, b) Close up of thermal paste mounted sample on board. 15

Figure 2.6: a) Multi-Layer layout view of Sample PCB on Altium, b) 3D Layout view of Sample PCB on Altium. 16

Figure 2.7: a) Multi-Layer layout view of advanced cooling PCB on Altium Designer, b) 3D Layout view of advanced cooling PCB on Altium Designer. 17

Figure 2.8: Example of a fabricated ITO/STO sample. 18

Figure 2.9: a) Visual of experimental set-up for I-V characterizations on device, b) Keithley Model 2612B SourceMeter used for characterization. 19

Figure 2.10: Example of Current vs. Voltage relation of ITO/STO sample 201 & the corresponding temperature. 20

Figure 2.11: FLIR ETS320 thermal camera used for thermal analysis. 21

Figure 2.12: FLIR Tools + software used for thermal analysis and data acquisition. 22

Figure 2.13: a) ITO/STO COMSOL temperature map simulation from section 2.2 under a 30mA bias, b) Temperature map of ITO/STO with FLIR thermal camera at 30mA bias. 23

Figure 3.1: THz-TDS purgeable measurement enclosure in the THz lab room 121. 26

Figure 3.2: Diagram of THz-TDS measurement system. 26

Figure 3.3: Image and table of calibrated system according to Tera K15 manual for PCA and TPX50 lens alignment to achieve the best THz signal amplitude. 28

Figure 3.4: Experimental set-up for knife-edge experiment for the beam focusing characterization. 29

Figure 3.5: Measured THz signal during the knife-edge sweep, and the corresponding fitted Gaussian error function to determine the beam radius. 31

Figure 3.6: Resulting beam diameter versus relative focusing length of the knife-edge experiment..... 32

Figure 3.7: Measured purged THz signal intensity (red line) in comparison to the noise intensity (faded line). Noise mean (black line) smoothed with frequency domain filter; this data is used to find system DNR & SNR..... 33

Figure 3.8: Simple diagram of THz measurements on STO/ITO sample..... 34

Figure 3.9: a) Measured time-domain THz pulse tunable response under increased applied biasing, b) Corresponding Fourier transform of time-domain measurements. 35

Figure 3.10: Extracted tunable refractive index and extinction coefficient of STO vias biasing from 0-45V..... 37

Figure 3.11: Experimental set up of Fourier-transform infrared spectroscopy system, b) Sample placement on FTIR during infrared measurements. 40

Figure 3.12: Measured reflectivity spectra from 1.5 μm to 17 μm under biasing from 0-50mA. 41

Figure 3.13: Calculated apparent refractive index vs wavelength from 1.5 μm to 17 μm under different bias conditions and zoomed plot from 6 μm to 10 μm 42

Figure 4.1: a) Top view HFSS model of the Au coplanar waveguide on STO, b) rear view of CPW sample with 3mm wide ITO strip (light blue). 47

Figure 4.2: Simulated S-parameters of CPW STO design, a) S21 (transmission) & b) S11 and S22 (reflection). 49

Figure 4.3: Fabricated coplanar waveguide STO sample. 51

Figure 4.4: HFSS 3D model of PCB CPW design, the orange material is copper, and the green material represent the FR-4 Substrate. 53

Figure 4.5: Calculated coplanar waveguide parameters using Keysight ADS LineCalc tool. 54

Figure 4.6: a) Simulated input reflection coefficient (S11) & output reflection coefficient (S22) of PCB CPW design, b) Simulated forward transmission coefficient (S21) & reverse transmission coefficient (S12) of PCB CPW design. 55

Figure 4.7: Final PCB layout for the fabricated guided device, allowing for repeatable measurements on the tunable effects of STO. 56

Figure 4.8: a) Anritsu MS46122A vector network analyzer used for RF measurements, b) SOLT calibration kit used for experimental set-up..... 58

Figure 4.9: ITO/STO device during VNA measurements mounted in custom 3D-printed PCB holder. 59

Figure 4.10: STO CPW device measurements under no induced thermal bias S-parameters, a) S21 (transmission) & b) S11 and S22 (reflection). 60

Figure 4.11: a) S21 (transmission) of the straight and wire bonded test ports, b) measured S11 and S22 (reflection) of the straight and wire bonded test ports 61

Figure 4.12: a) Measured S-parameters from 0mA to 25mA biasing on the back side ITO heating film. 63

1 Introduction

1.1 Tunable Electromagnetic Materials

Tunable electromagnetic materials are materials whose electrical, optical, or dielectric properties can be modified through an external stimulus. Instead of relying on fixed geometry, these materials allow the electromagnetic response of a structure to change through applied voltage, temperature, optical excitation, or other control mechanisms. This is essential for reconfigurable electromagnetic systems where transmission, reflection, absorption, phase, or resonance behavior must be tuned dynamically.

Ferroelectric and high-permittivity oxides are significant group in tunable electromagnetic materials. Materials such as barium strontium titanate (BST) exhibit electric field dependent permittivity, which allows for tunable capacitors, phase shifters, filters, and matching networks. BST is especially relevant to microwave systems because its dielectric constant is tunable with applied bias, making it possible to tune circuit behavior without mechanically changing the device structure [1]. Thin-film BST capacitors have demonstrated significant capacitive tuning at low DC bias, with reports of approximately 60% tunability at 7 V, making BST attractive for compact tunable radiofrequency (RF) systems [2].

Liquid crystals are another widely studied tunable material system, typically in terahertz and optical applications. Liquid crystals have an anisotropic refractive index, which changes when the molecules are reoriented by external electric or magnetic fields. This tunable control and its change in refractive index can be used to tune phase delay, polarization, and resonances. Liquid crystal THz phase shifters have demonstrated full 360° phase control near 1 THz, showing that this material class can provide significant tunability [3]. However, typical liquid crystal devices

often require tens to hundreds of micrometers of crystal thickness, which increases loss and slows the tuning response.

Two-dimensional materials, most commonly graphene, have become very significant for tunable electromagnetic systems. Graphene has an adjustable conductivity with electrostatic gating, allowing for tunable electromagnetic response electrically. Graphene is frequently used in the THz range, where it can be combined with resonant structures to improve the interaction between the material and incident waves. Graphene THz modulators have shown very large modulation depth with only a small change in Fermi level, which demonstrates the capabilities and significance of tunable two-dimensional materials [4]. The main challenges are the weak interaction of a single layer with free-space waves, which often requires integration into local field enhancing structures, as well as limited reproducibility caused by fabrication variations such as non-uniform films, defects, wrinkles, and other non-idealities involved in the fabrication process.

Another common tunable material is vanadium dioxide (VO_2), which is commonly studied because it undergoes an insulator to metal transition, producing a large change in conductivity that strongly modifies terahertz and infrared responses [5]. Chalcogenide phase-change materials such as germanium antimony telluride (GST) are also useful because they can switch between amorphous and crystalline phases whilst maintaining the selected state without continuous power [6]. Phase change materials are very beneficial as tunable electromagnetic devices, but require precise control of either an optic, electrical, or thermal switching mechanism.

1.2 Motivation

The previous section discussed the various common material systems for achieving a tunable electromagnetic response. Many of these tunable devices are designed around a specific frequency range, which can make it difficult to compare material behavior across RF, terahertz,

infrared, and optical regimes. This motivates the study of a material platform where the same underlying tuning mechanism can be examined across multiple frequency bands.

Strontium titanate ($SrTiO_3$, STO) was chosen for this study because its dielectric and optical properties are strongly influenced by sample temperature. Instead of relying on separate electrical, mechanical, or optical tuning mechanisms for each frequency range, this thesis investigates whether controlled heating can be used to modify the electromagnetic response of STO material platforms. This approach is not intended for high speed tunability, but it provides a practical way to study thermally induced changes in transmission, refractive index, permittivity, across different frequency ranges.

Therefore, the motivation of this thesis is to develop and evaluate thermally controlled STO device platforms to be measured across infrared, THz, and radio frequency regimes. By using ITO as a conductive layer for Joule heating, localized temperature changes can be introduced into STO samples while the terahertz, infrared, and microwave responses are measured. This allows the thermal tunability of STO to be studied experimentally and provides a foundation for future thermally reconfigurable electromagnetic devices.

1.3 Materials Systems

1.3.1 Strontium Titanate Material Overview

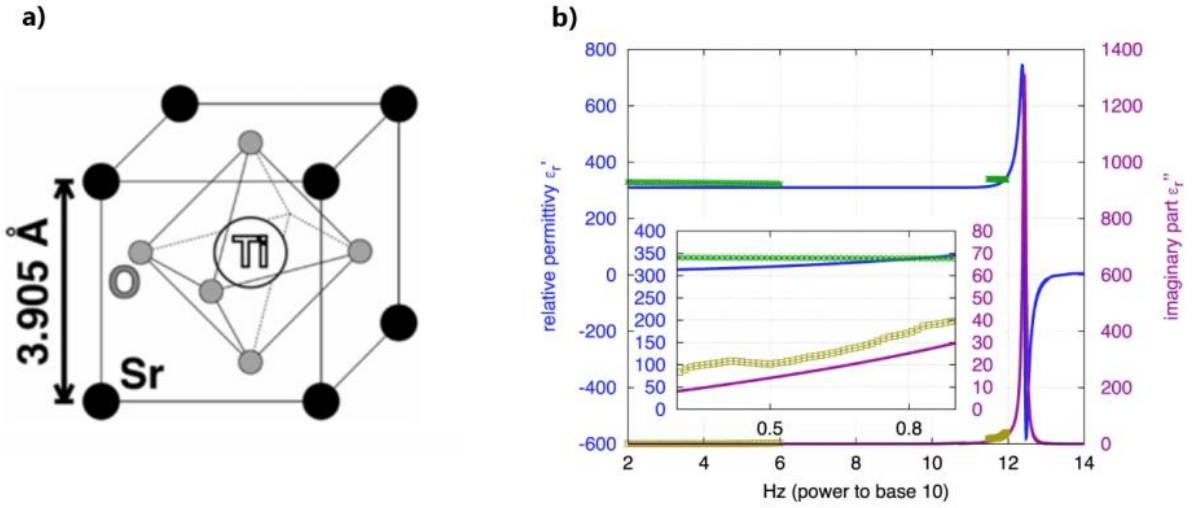


Figure 1.1: a) Crystal structure of cubic $SrTiO_3$ showing the Sr, Ti, and O atomic positions. Reproduced from [7]. b) Relative and imaginary permittivity of STO from 10^2 to 10^{14} Hz reproduced from [8].

Strontium titanate, STO, is a high permittivity oxide material widely studied for its electronic, RF, microwave, and terahertz applications. For example, single crystal STO has been reported to have a relative permittivity in the order of 300 at microwave frequencies [9]. This high permittivity makes STO sensitive to dielectric tuning, where induced temperatures lead to changes in permittivity and refractive index of the material. However, this same property also creates practical tradeoffs, including dielectric loss and waveguide geometry constraints, which are discussed later in this thesis.

The strong low-frequency response of STO is connected to its lattice structure behavior. In the terahertz region, the tunable dielectric response is influenced by polar phonon modes, this includes a transverse optical soft mode that significantly contributes to the material's permittivity [10]. Polar phonons are lattice vibrations that induce oscillating electric dipoles because positive and negative ions move relative to each other, allowing them to strongly interact with

electromagnetic waves. This is an essential aspect of this thesis because the thermally tunable response of STO can produce a much larger response in the THz regime than would be expected from a simple tunable optical parameter response. Previous literature shows STO's measurable temperature-dependent optical properties from 450-1600 nm. Toyoda and Yabe studied the refractive index of STO changes with temperature over the visible frequency range [11]. This thermally tunable response is useful as supporting literature for the visible and infrared responses of STO under thermal bias.

Induced thermal strain is another important factor because lattice distortion can modify the dielectric behavior of STO. Previous work shows that strained STO films can exhibit strongly altered ferroelectric and dielectric properties at room temperature [12]. In this thesis, strain is induced from the localized heating using thin-film heating which can introduce thermal gradients and nonuniform thermal expansion in the STO substrate. This material's unique characteristics and response to temperature variation is the basis of the tunable electromagnetic studies of this thesis.

1.3.2 Indium Tin Oxide Material Overview

Indium tin oxide is a transparent conductive material which is typically used in optic devices, as transparent electrodes, and as thin film heaters. ITO is formed by doping indium oxide, InO, with tin, which gives the material the significant combination of electrical conductivity and optical transparency [13]. The benefit of using ITO over other conductors is that ITO can conduct current as a thin film, while still allowing partial optical access.

The electrical and optical properties of ITO are mainly controlled by film thickness and fabrication processes. Conductivity of ITO improves with thickness, but it can directly reduce optical transmission [14]. This balance between conductivity and transparency is what makes ITO

useful in applications where electrical access is needed without interfering with or blocking electromagnetic interaction with the sample. ITO's compatibility with thin film deposition and patterning also makes it practical for integration into device structures.

In this thesis, ITO is used as a polycrystalline conductive layer for Joule heating of the STO sample. When a voltage is applied across the ITO film, current flows through its finite sheet resistance and generates heat through resistive power dissipation. This allows the ITO layer to act as a distributed thin film heater over the STO surface. ITO is perfect for this project because its sheet resistance can be engineered through film thickness and fabrication techniques, allowing the film to support current flow while still producing measurable heating under applied bias [15].

1.4 Research Objectives and Thesis Scope

1.4.1 Research Objectives

The first objective is to design and evaluate thermally controlled STO device structures using a thin conductive oxide layer, ITO. This conductive layer is used to apply electrical bias and generate localized heating across the STO substrate. COMSOL simulations are used to study the temperature distribution, thermal gradients, and expected heating behavior before fabrication.

The second objective is to fabricate, prototype, and characterize the thermally controlled samples and devices that enable experimental work in this thesis. This stage is essential because the infrared, THz, and RF measurements require samples that can be reliably biased, contacted, and mounted in measurement setups. Device fabrication defines the material structure, patterned geometry, and electrical contacts needed for device operation, while wire bonding and prototyping design platforms provide the ability to control and measure the sample response. Biasing and thermal measurements are then used to verify that the samples produce reliable heating behavior

and measurable thermal gradients laterally across the STO substrate. This work establishes the experimental platform required for the optical and RF studies presented in later chapters.

The third objective is to characterize the infrared and terahertz response of thermally controlled STO based devices. Terahertz time-domain spectroscopy (THz-TDS) is used to measure changes in transmitted pulse delay and frequency domain response, allowing changes in refractive index and permittivity to be evaluated. Further experimentation in the IR measuring reflectivity is included to examine the broader electromagnetic response of the thermally controlled oxide structures.

The fourth objective is to investigate guided wave RF structures fabricated on STO. Coplanar waveguide devices are designed, simulated, fabricated, and measured to study how the thermal response of STO affects reflection and transmission at radio frequencies. The goal is to use Vector Network Analyzer (VNA) to carefully observe the changes in S-parameter response of the device in respect to induced heating of the sample.

1.4.2 Thesis Scope and Organization

The scope of this thesis is focused on thermally controlled STO based devices and their electromagnetic response. This work emphasizes material tunability, where temperature and thermal gradients modify the properties of STO and influence electromagnetic tunability across various frequency bands. Overall, this thesis emphasizes the work involving thermal simulation, device fabrication, measurement setup development, and experimental characterization and tunable response analysis.

This thesis is organized into five chapters. Chapter 1 introduces the motivation and material background for STO and ITO. Chapter 2 focuses on experimental development and preliminary analysis for the devices biased with different conductive thin films (ITO/STO). This includes

COMSOL simulations, device fabrication, printed circuit board (PCB) design & prototyping, I-V measurements, and thermal characterization. Chapter 3 presents thermally controlled optical measurements and tunable responses across frequency ranges, including the THz and infrared response. Chapter 4 focuses on a guided wave device, including coplanar waveguide (CPW) design on ITO/STO, PCB prototyping and design, RF measurement integration, S-parameter measurements, and de-embedding. Chapter 5 summarizes the main findings and discusses future work.

2 Development of Thermally Controlled Device Platforms

2.1 Introduction & Overview

This chapter presents the development of thermally controlled STO based device platforms used for experimental work in this thesis. The purpose of this chapter is to describe how the samples were designed, simulated, fabricated, and thermally analyzed before being used in later optical frequency measurements. Since the tunable electromagnetic responses are analyzed in chapter 3-4, this chapter focuses on the essential processes required to create reliable thermally tunable devices.

The device concept is based on using ITO as a conductive oxide layer deposited on to STO to generate localized heating through electrical biasing. This behavior can be studied experimentally, but the samples must first demonstrate stable electrical contact, repeatable heating, and a measurable thermal profile. This chapter serves as the experimental foundation for the rest of the thesis. COMSOL simulations are used to analyze the thermal profile of the device and guide the geometry before fabrication. Fabrication and PCB design are then used to produce physical samples with conductive regions that can be biased and mounted for testing. Wire-bonding provides the electrical interface between the small oxide samples and the external measurement boards, allowing the devices to be integrated into practical measurement setups.

This chapter concludes with preliminary I–V and thermal measurement analysis used to quantify device operation. I–V and thermal measurements are used together to establish the relationship between electrical biasing and thermal response, where the measured current defines

the input heating conditions and the corresponding thermal measurements quantify the resulting temperature change and spatial heating profile across the sample.

2.2 COMSOL Simulations

COMSOL Multiphysics was used to model and simulate the thermal behavior of the device structures before fabrication and experimental testing. These simulations provide a way to estimate heat generation, temperature distribution, and thermal gradients produced by electrical biasing of ITO. This was essential for evaluating how device geometry, material layout, and PCB integration could influence the heating profile across the STO substrate. The COMSOL results were used as a design tool to guide sample layout and support the development of measurable devices for later electromagnetic experiments.

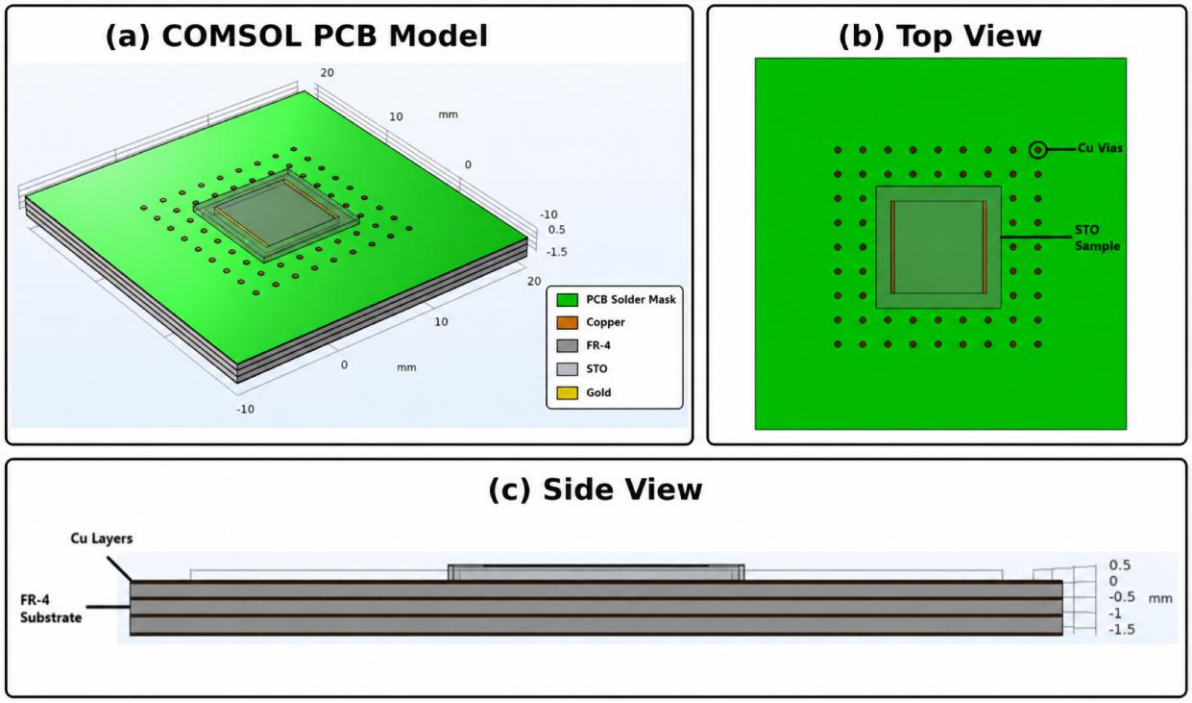


Figure 2.1: COMSOL 4-layer PCB model geometry for the thermally controlled STO sample platform, (a) the full 3D PCB model, (b) the top view layout with copper vias and central STO sample, and (c) the side view cross section of the copper layers and the composite substrate, FR-4.

This COMSOL PCB model was developed to evaluate how the printed circuit board structure influences heat flow from the thermally controlled STO sample. The modeled PCB consists of an FR-4 substrate with embedded copper layers and copper vias, as shown in Fig. 2.1. These copper features are important because they provide a thermal path away from the sample and influence how heat spreads through the board during electrical biasing. The STO sample is modeled as a 10 mm x 10 mm substrate positioned over an 8 mm x 8 mm opening in the PCB, which is required to allow optical or terahertz transmission through the sample. The sample rests on copper contact regions around the opening, allowing the PCB copper layers to act as a thermal dissipation path.

The COMSOL simulations were implemented using electric currents and heat transfer physics in solids to integrate electrical biasing with thermal response. A terminal and ground boundary were assigned across the conductive 20 nm thick ITO region for biasing, while remaining boundaries were treated as insulated. The resulting Joule heating from the applied current distribution was used in the heat transfer model as the tunable thermal source for the STO sample. Thermal insulation, heat flux, and temperature boundary conditions were then used to represent heat transfer and external heat exchange. A dense and high-quality element mesh was important to this simulation to properly simulate the thin-film geometry and the localized temperature response of the PCB model.

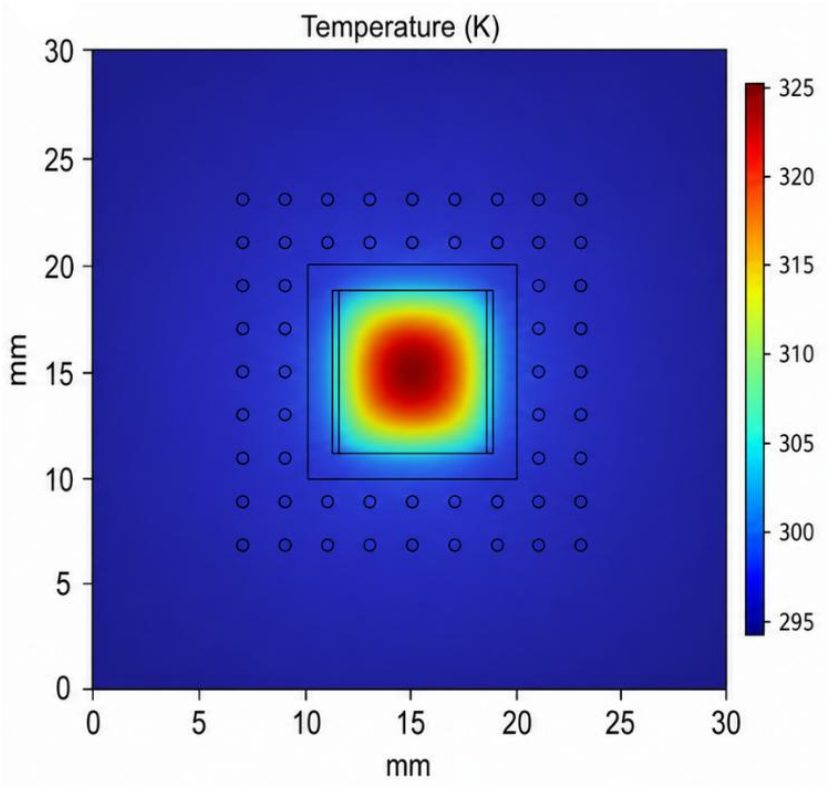


Figure 2.2: Resulting temperature profile from COMSOL simulation of ITO/STO via a 30 mA bias.

A key design goal was to improve the thermal gradient across the STO sample while maintaining a practical PCB geometry for measurement. Since STO tunability is driven by temperature-dependent material properties, the temperature distribution across the sample directly affects the expected electromagnetic response. Therefore, the PCB was not treated only as a mechanical holder or electrical interface, but as part of the thermal design. The copper layers, vias, and contact geometry were analyzed to determine how effectively heat could be removed from the sample edges and the extent of the thermal gradient that could be generated across the active region.

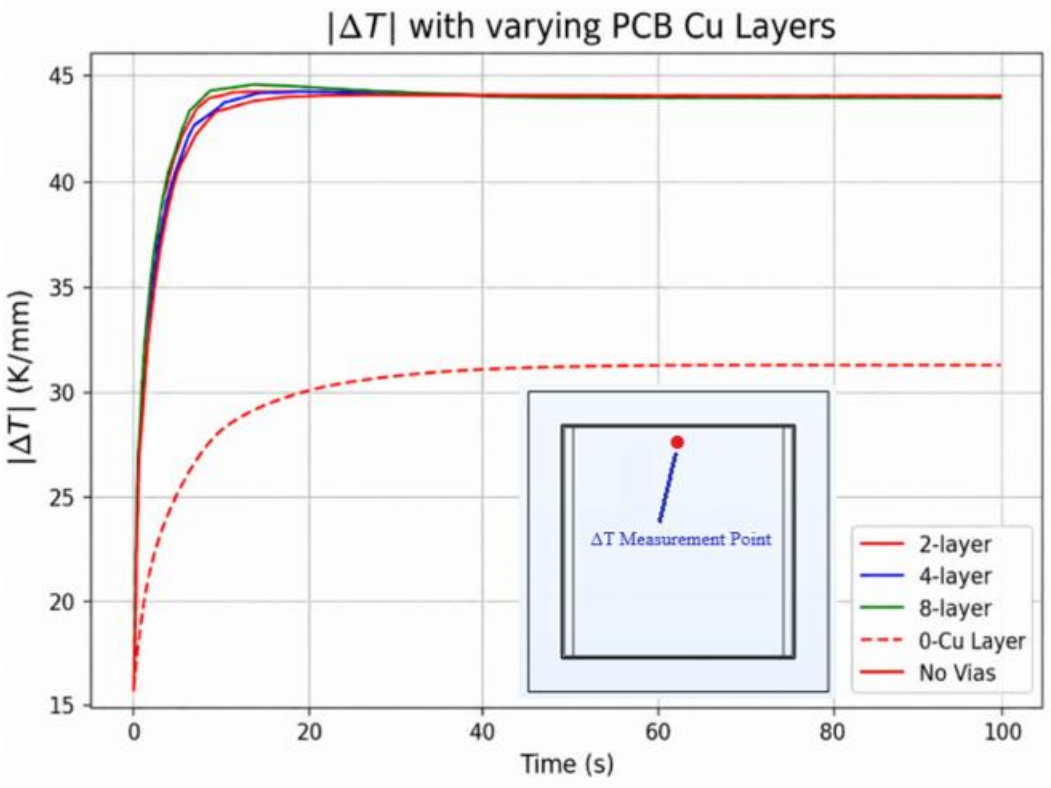


Figure 2.3: Simulated lateral thermal gradient response of the STO sample for different PCB copper layer configurations. All simulations used a 7.5 mm × 7.5 mm ITO heating electrode biased at 30 mA, with the inset indicating the lateral ΔT measurement location used for comparison.

The effect of PCB copper-layer count was first observed by comparing simulated temperature gradient behavior for different board configurations. As shown in Fig. 2.3, cases with copper layers reach a steady thermal gradient of approximately 44 K/mm, while the PCB case without copper layers reaches only about 31 K/mm. This shows that copper in the PCB is essential for improving heat dissipation and increasing the thermal gradient response across STO. However, the simulations also show that increasing the number of copper layers from two to four or eight layers does not produce a significant additional improvement. All copper layer cases approximately reach the same gradient in steady state, indicating that the presence of copper is more essential than introducing a larger thermal channel with more copper layers.

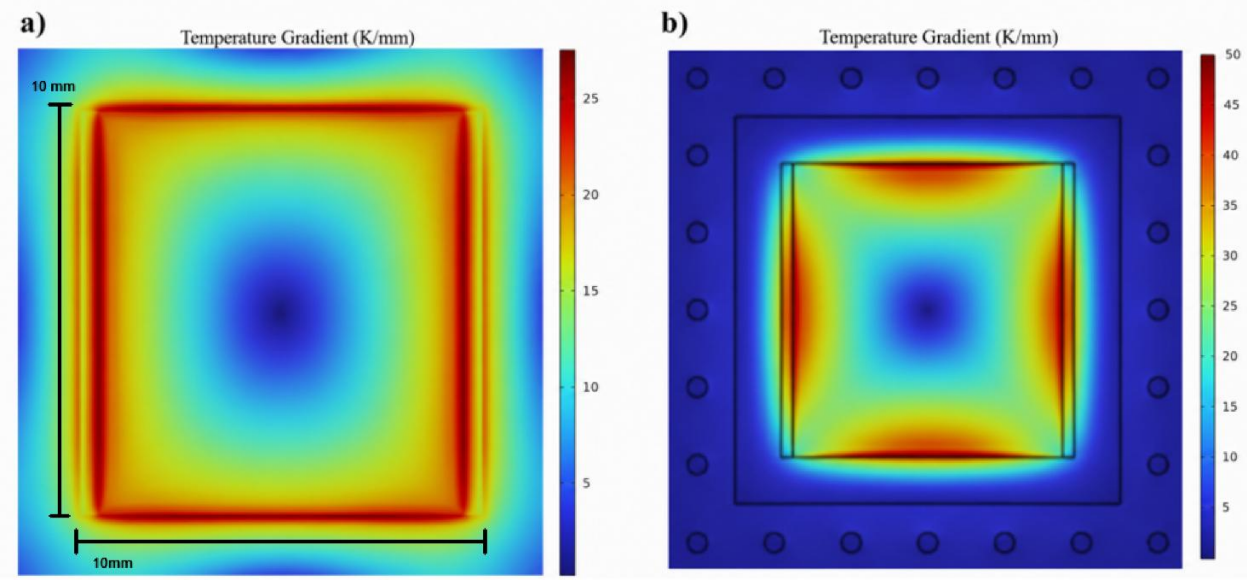


Figure 2.4: Simulated thermal gradient magnitude across the STO sample for two contact configurations: (a) STO without Cu contacts and (b) STO with Cu contacts. The results illustrate the effect of Cu contacts on the spatial thermal-gradient distribution across the sample.

The contact geometry between the STO sample and the PCB also has a significant effect on the simulated thermal gradient. Without copper contact regions around the STO sample, the maximum thermal gradient does not exceed 27 K/mm, with the highest gradients concentrated near the sample perimeter, as shown in Fig. 2.4. In comparison, when the STO sample is placed on copper contacts connected to the PCB copper layers, the simulated maximum thermal gradient increases to 50 K/mm. This design provides a much stronger localized gradient across the STO region, with peak values approaching approximately 50 K/mm in the simulated map. This improvement occurs because the copper contacts provide efficient heat extraction near the sample edges, increasing the temperature difference across the STO substrate.

These simulations demonstrate that the PCB design has a direct effect on the thermal tunability of the STO platform. The copper layers and contact regions are necessary for producing a sufficient thermal gradient. Based on this analysis, the PCB design requirements were refined to include copper contact regions and internal copper layers while preserving the central transmission

window needed for optical and terahertz measurements. This thermal modeling and simulation were essential for guiding the PCB design toward a geometry that could provide effective heat dissipation, support strong thermal gradients, and improve the expected tunability of the STO platform. The detailed PCB layout and implementation of these design requirements are described in the following section.

2.3 Prototype PCB Design and Device Integration

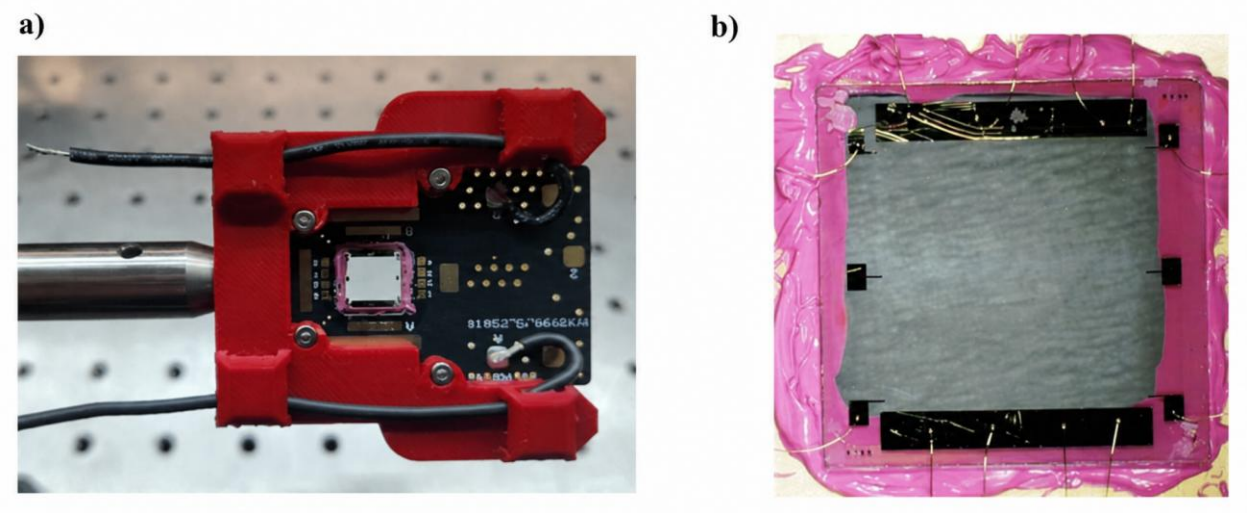


Figure 2.5: a) Device set-up in 3D printed PCB holder, b) Close up of thermal paste mounted sample on board.

The PCB designs were designed on Altium to provide a practical interface between the thermally-controlled STO sample and external measurement equipment. Essential design requirements were electrical biasing, mechanical sample support/mounting, thermal dissipation from sample, and optical access through the center of the sample. The STO sample is mounted over an 8 mm x 8mm opening, allowing transmission measurements and spatial scanning across the sample area. Copper contact regions around the opening support the sample while providing a thermal path into the PCB copper layers when paired with thermal paste. Screw holes were included for mounting the board into 3D-printed holders for repeatable positioning during testing

(Fig. 2.5). Additionally, ENIG surface finish was essential on the exposed metal regions to support wire bonding, since the thin gold surface provides a reliable wire bonding contacts.

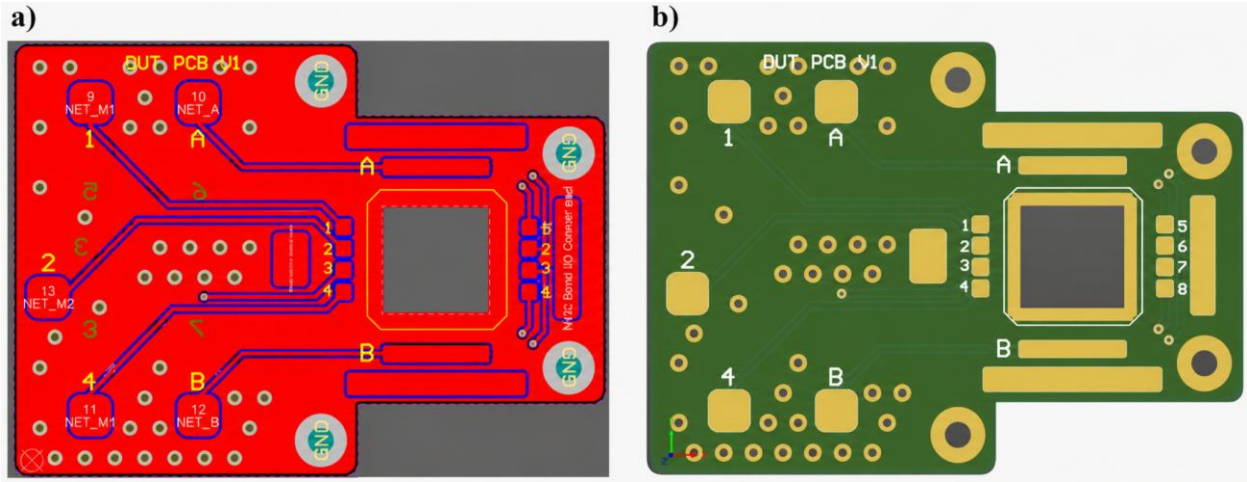


Figure 2.6: a) Multi-Layer layout view of Sample PCB on Altium, b) 3D Layout view of Sample PCB on Altium.

The first prototype PCB layout is shown in Fig. 2.6. The main biasing pads, labeled A and B, provide the primary electrical connections used to apply voltage across the sample. Additional biasing pads are placed along each side of the sample region to provide more flexibility during probing, wire bonding, and device testing. These extra contact points allow different biasing configurations to be accessed if the primary pads are not ideal for a specific sample or measurement setup. The board also includes scattered copper vias, which connect the copper layers through the FR-4 substrate and improve thermal spreading through the PCB. These vias help link the top copper contact regions to the internal copper layers, supporting the heat dissipation behavior modeled in the COMSOL simulations.

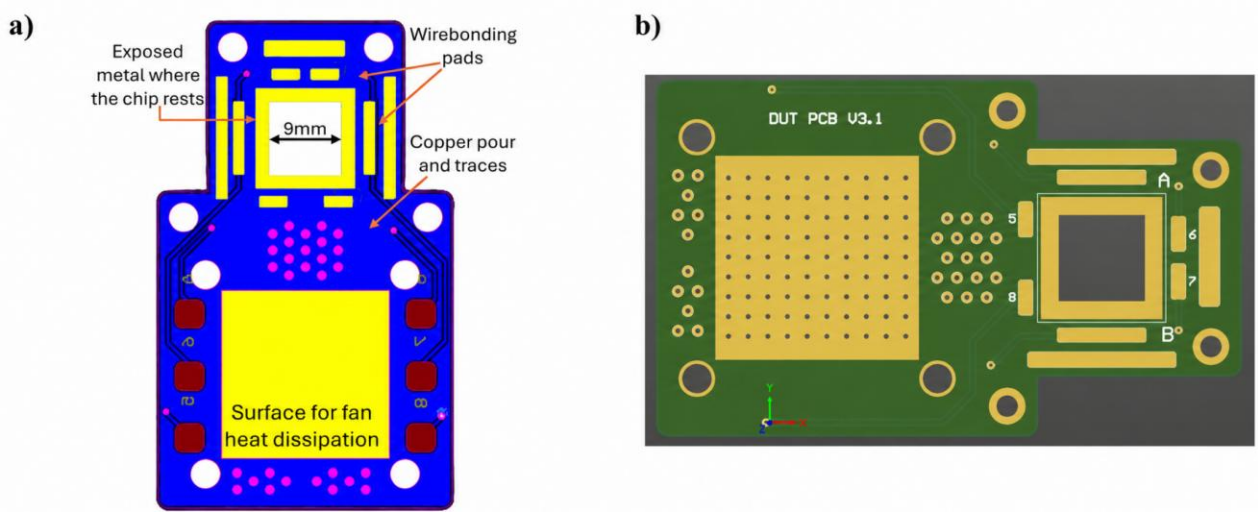


Figure 2.7: a) Multi-Layer layout view of advanced cooling PCB on Altium Designer, b) 3D Layout view of advanced cooling PCB on Altium Designer.

A second PCB design was also developed to improve thermal management, as shown in Fig. 2.7. This design keeps the same general design as Fig 2.6 but adds a large, exposed copper surface on the PCB. The exposed copper region provides a mounting area for a thermoelectric cooler, heatsink, or fan type cooling structures. This gives the setup the option to increase heat dissipation through the PCB during extended measurements or high current operation. While the first design is sufficient for basic sample biasing and transmission measurements, the second design provides additional flexibility for experiments where more stable temperature control or stronger heat removal is needed.

The PCB designs are a critical part of the thermally controlled STO device platform. It provides electrical contact, mechanical support, experimental access, and thermal dissipation needed to operate the designed devices. By combining all the needed requirements into this design, the PCB enables the STO samples to be integrated into multiple experimental setups. This makes the board an essential link between the simulated thermal design and the electromagnetic measurements in later chapters.

2.4 Sample Fabrication

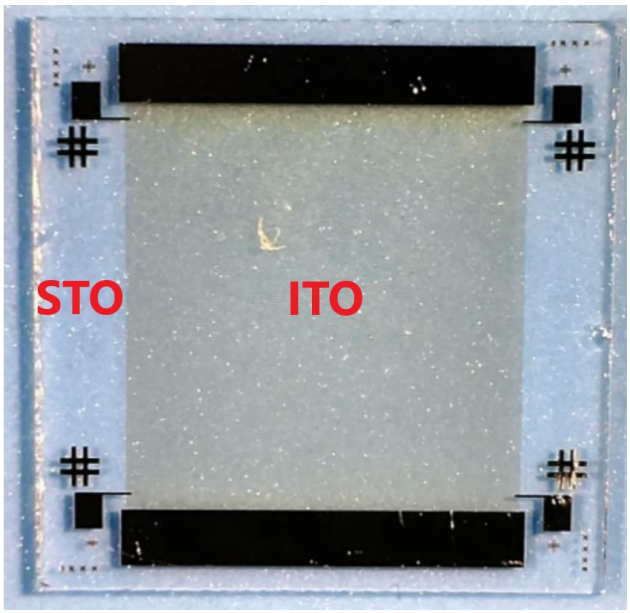


Figure 2.8: Example of a fabricated ITO/STO sample.

The device fabrication described in this section was carried out at the UC Davis Center for Nano-MicroManufacturing (CNM2) by a project collaborator. The fabrication details were provided by the collaborator who performed the CNM2 processing. Producing a high-quality sample is fundamental to this work, as it enables systematic characterization of the thin film's performance and thermal tuning properties.

The ITO/STO samples were fabricated using a two-step process consisting of the ITO heating channel followed by metal bias pads. The starting substrate was a 10 mm × 10 mm STO chip. Before lithography, the substrate was dehydrated on a hotplate to remove surface moisture and improve photoresist adhesion. A negative photoresist was then spin-coated onto the STO surface and patterned using optical lithography to define the ITO heating region near the center of the sample. After lithography, the ITO thin film was deposited using sputtering to a thickness of approximately 20 nm. Lift-off was then performed to remove the excess ITO outside the patterned region, leaving only the central heating channel on the STO surface.

A second lithography step was used to define the metal contact pads for electrical biasing. Since gold does not adhere strongly to STO by itself, a thin titanium adhesion layer was deposited before the gold layer. The final contact stack consisted of gold metal pads placed at opposite ends of the ITO channel, with the gold layer providing a conductive contact surface. After metal deposition, lift-off was used to remove unwanted material and complete the patterned contact structure.

The completed ITO/STO samples consisted of a thin patterned ITO heating channel connected by Ti/Au bias pads on the STO substrate. This structure allowed current to be applied through the ITO layer, producing localized Joule heating across the sample. The fabrication process therefore provided the physical basis for connecting electrical biasing to controlled thermal tuning in the STO devices characterized throughout this thesis.

2.5 I-V Analysis

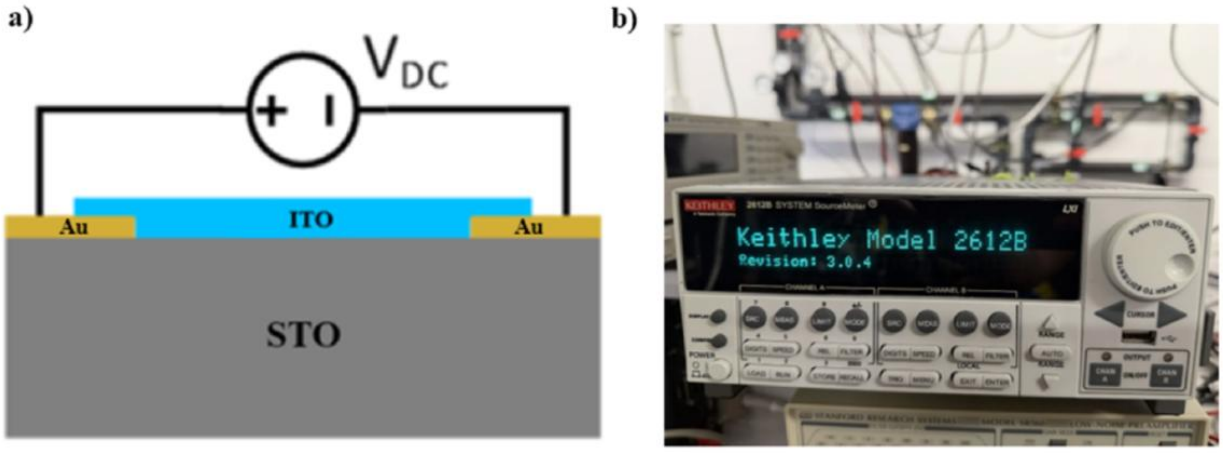


Figure 2.9: a) Visual of experimental set-up for I-V characterizations on device, b) Keithley Model 2612B SourceMeter used for characterization.

I–V measurements were performed to characterize the critical electrical behavior of the thermally controlled device samples before using them in later electromagnetic measurements. Since the tuning mechanism depends on Joule heating, it was important to first determine how

each device responds to applied bias and what tunable range could be used reliably. The electrical characterization was performed using a Keithley 2612B Source Meter, which is known for its precision testing capabilities. This was used to sweep the applied current while recording the necessary voltage across the sample, to ensure material integrity and stable temperature control across the tuning range.

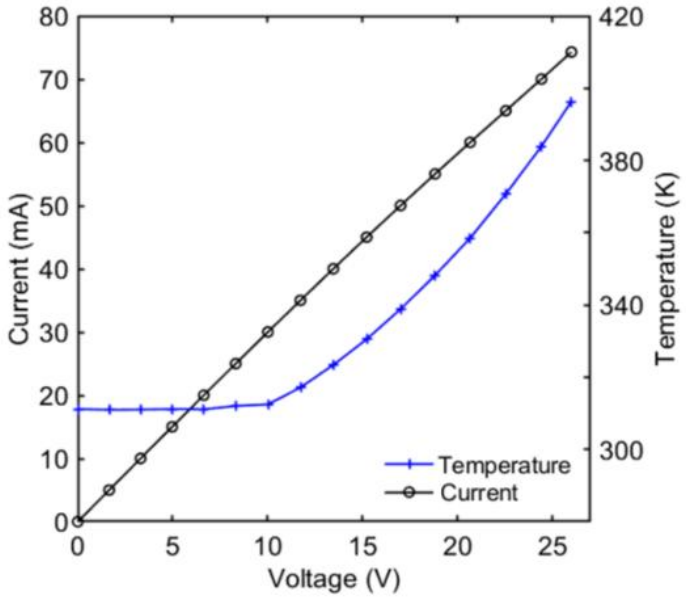


Figure 2.10: Example of Current vs. Voltage relation of ITO/STO sample 201 & the corresponding temperature.

For the ITO/STO device, the I–V measurement is especially important because the ITO layer serves as the resistive heating element. As shown in Fig. 2.10 the device exhibits an approximately linear current response over the measured bias range, confirming that the fabricated ITO film behaves as a stable controlled conductive heating layer. The corresponding temperature was found during thermal analysis, characterizing the applied bias through the ITO layer in respect to the produced Joule heating. This behavior helps define an operating range where the device can generate useful temperature changes without showing signs of electrical instability.

2.6 Thermal Analysis

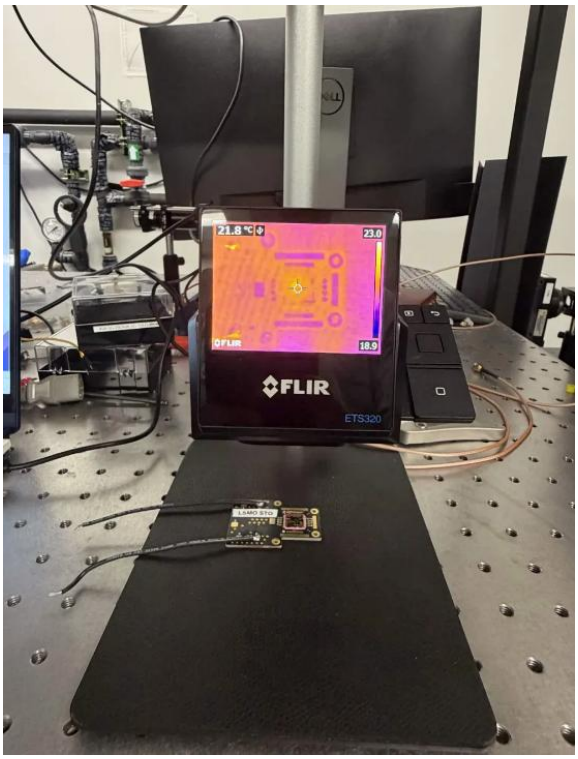


Figure 2.11: FLIR ETS320 thermal camera used for thermal analysis.

Thermal analysis was performed to measure the temperature profiles produced by electrical biasing of the tunable device platforms. While the I–V measurements define how each sample responds electrically, thermal imaging shows how that electrical input is converted into spatial heating across the sample. This step is essential because the tunable response studied in later chapters depends on temperature-dependent changes in the STO devices, and direct correlation between temperature and tunable response cannot be quantified without these measurements.

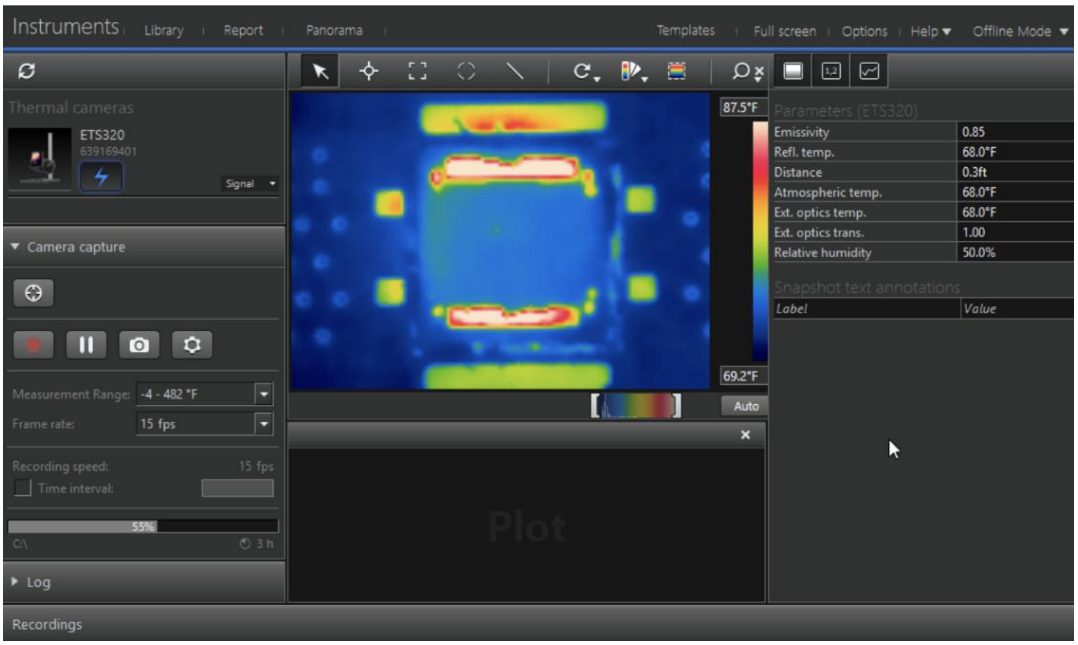


Figure 2.12: FLIR Tools + software used for thermal analysis and data acquisition.

The thermal measurements were collected using a FLIR ETS320 thermal camera with 170 µm per pixel resolution (Fig. 2.11) and analyzed through the FLIR Tools+ software interface (Fig. 2.12). During measurement, the sample was mounted on the PCB and biased using the same setup described in the I–V analysis. The resulting temperature distribution caused from biasing the sample was then captured from the top surface of the sample. Several experimental parameters were kept fixed during testing so that the measured thermal response is accurate. The emissivity was set to 0.85, the camera distance was set to approximately 0.3 ft, and the reflected, atmospheric, and external optics temperatures were set near room temperature. Emissivity during this analysis was very important because thermal cameras calculate temperature from the infrared radiation emitted by a surface, and emissivity depends on how a surface radiates compared with an ideal black body [16]. The chosen emissivity value is also consistent with reported emittance values for strontium titanate ceramic coatings, which were measured from 0.8–0.86 depending on coating

thickness [17]. Although the exact emissivity can vary with fabrication and the surface conductor ITO, 0.85 was chosen because this matched the current room temperature best under no bias.

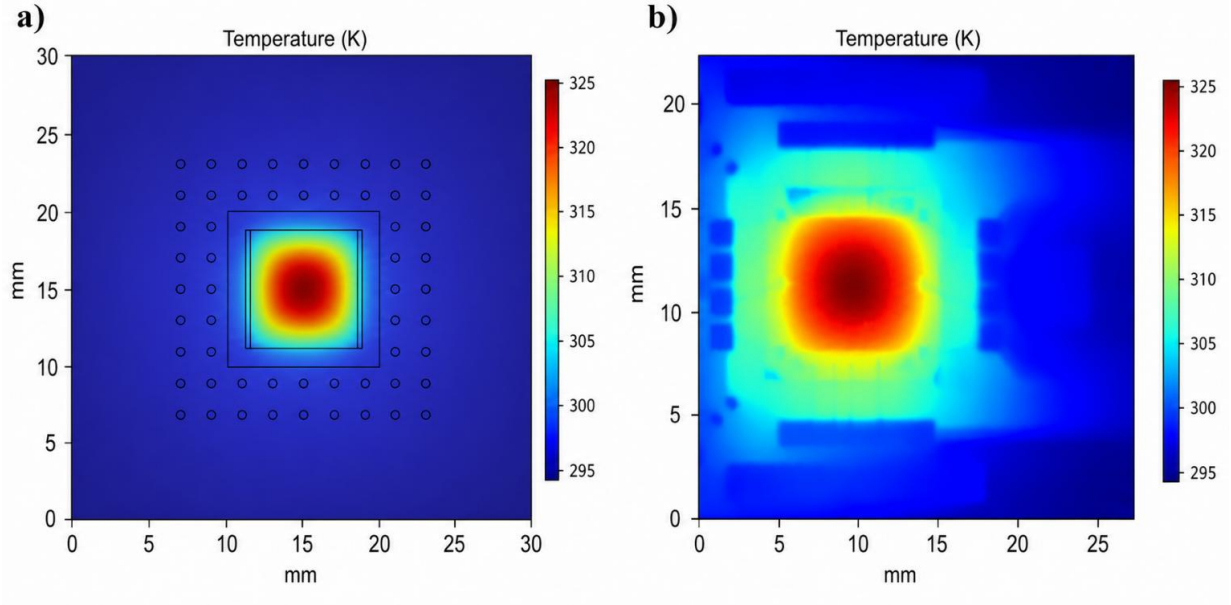


Figure 2.13: a) ITO/STO COMSOL temperature map simulation from section 2.2 under a 30 mA bias, b) Temperature map of ITO/STO with FLIR thermal camera at 30 mA bias.

The measured thermal maps provide a direct comparison between the fabricated device behavior and the COMSOL thermal model developed earlier in the chapter. For example, the ITO/STO structure temperature profile in comparison with the COMSOL simulations shown in Fig. 2.13 confirms that the device has the expected thermal profile across the sample. With heat retention of 5 K more in the PCB in comparison to simulation. This difference is most likely from experimental nonidealities with heat transfer, thermal paste, and sample to PCB contact. Even with these differences, the comparison shows that the PCB design and ITO heating configuration produce the intended localized thermal profile needed for later tunability measurements.

2.7 Summary

This chapter established the experimental platform used to study thermally controlled STO devices. The PCB design became more than a support structure; it is directly responsible to the

thermal behavior of the sample. The COMSOL simulations showed the essential geometry and board stack up necessary to achieve the desired thermal profile across the device. The fabricated PCB platforms provided a repeatable way to bias, mount, and thermally manage the STO samples during measurement. The I–V and thermal imaging results then confirmed the operating behavior of the devices and provided the temperature information needed to interpret later measurements. These platform level results are essential for the following chapters, where the thermally induced response of STO is analyzed and quantified using this data across terahertz, infrared, and radio-frequency experiments.

3 Thermally Controlled Optical Devices

3.1 Introduction & Overview

This chapter focuses on the thermally tunable response of STO at THz and infrared frequencies. The main objective is to examine how controlled heating changes the electromagnetic behavior of STO across different frequency ranges. This chapter investigates using temperature as a tuning mechanism that actively manipulates material response which directly impacts electromagnetic signals.

The first part of the chapter examines the terahertz response of STO. STO is particularly important in this work because its optical and dielectric properties are sensitive to temperature. Previous measurements have shown that the refractive index of STO changes with temperature, supporting the idea that heating can alter its propagation behavior [11]. In the THz experiments, this tunability is observed through changes in the transmitted pulse, including time-delay shifts and variations in the extracted refractive index. The second part of the chapter investigates the thermally tunable response of the STO configuration at infrared frequencies. There is limited research on the thermally tunable response of STO at infrared frequencies, the goal of this chapter is to investigate and characterize a potential tunable response in this frequency band.

3.2 Thermally Engineered STO: Terahertz Response

3.2.1 Section Overview

This chapter connects the essential device platform developed in Chapter 2 to the THz material response. The PCB design, sample mounting, I–V behavior, and thermal maps are principal foundations in performing and understanding the tunable response. In this system we experimentally gather and examine changes in THz pulse delay and extracted refractive index

under applied bias. This experimental analysis allows us to characterize the tunable response of STO at THz frequencies, but system characterization and calibration were essential before any tests.

3.2.2 THz-TDS System Overview

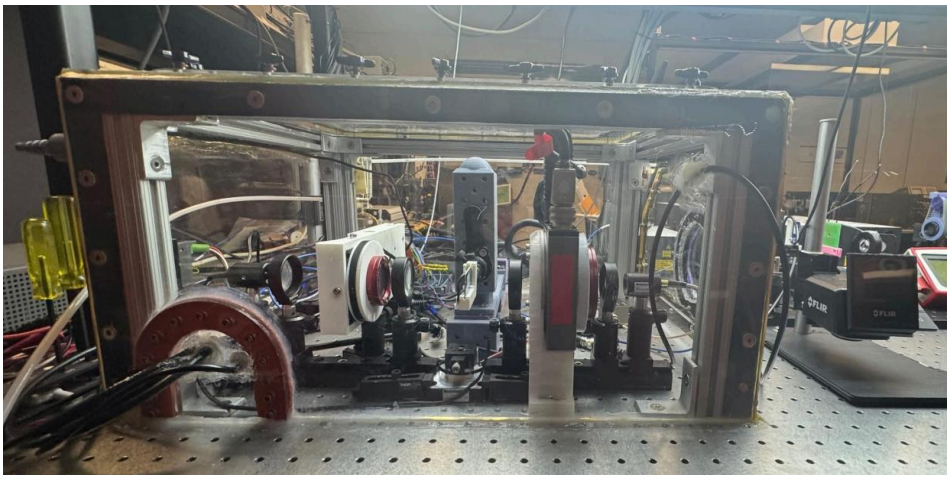


Figure 3.1: THz-TDS purgeable measurement enclosure in the THz lab room 121.

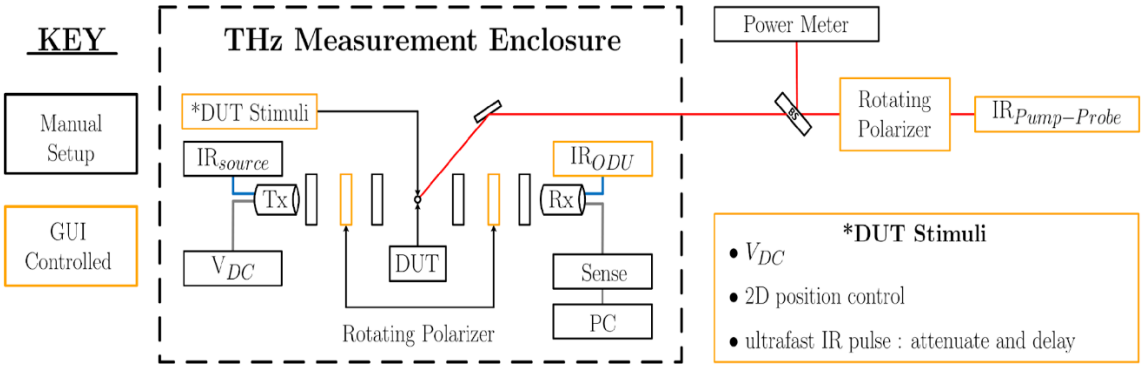


Figure 3.2: Diagram of THz-TDS measurement system.

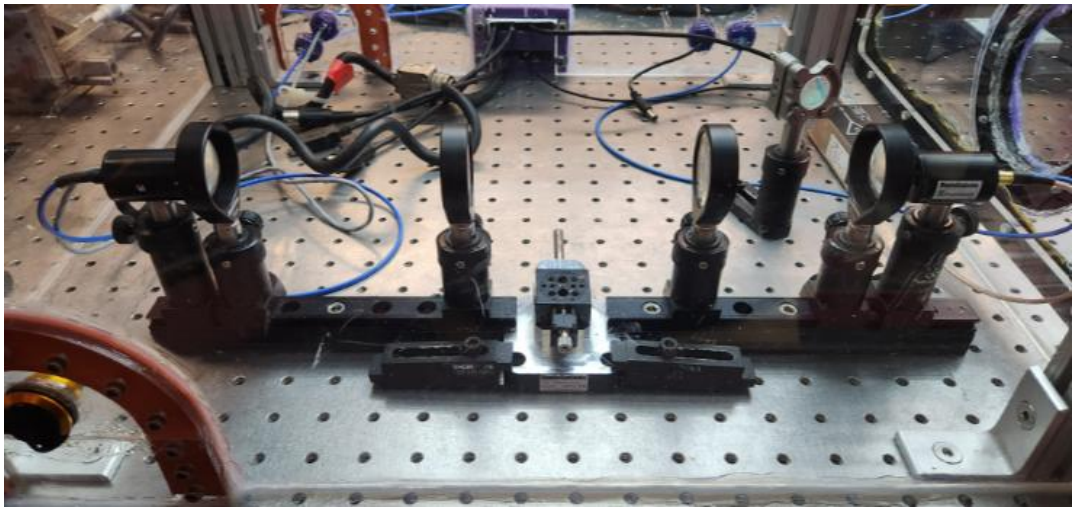
Terahertz time-domain spectroscopy (THz-TDS) is a measurement technique used to characterize materials in the terahertz frequency range. THz-TDS directly measures the transient electric field of a THz pulse as a function of time. Because both the amplitude and phase of the electric field are preserved, the measured waveform can be used to extract material properties such

as refractive index, absorption, conductivity, and permittivity [18]. A typical THz-TDS system is driven by an ultrafast femtosecond laser. The laser beam is split into two optical paths: one used to generate the THz pulse and the other used to detect it. In a photoconductive antenna (PCA) system the femtosecond laser shines on the semiconductor in the PCA producing a rapid transient current that emits a THz pulse [18]. The emitted THz pulse is then guided through the calibrated optical path and focused onto the sample. Where the resulting transmitted pulse is analyzed in time and frequency domain.

In this work, the THz-TDS system is used to measure the transmission response of STO under controlled thermal conditions. Since changes in the STO refractive index alter the propagation time and spectral response of the transmitted THz pulse, THz-TDS provides a direct method for evaluating the material's thermal tunability. Prior to these measurements, the system must be calibrated and characterized to ensure stable alignment, sufficient signal-to-noise ratio, and repeatable reference measurements.

3.2.3 THz-TDS System Calibration

Before collecting biased sample data, the optical path must be aligned to maximize the transmitted THz field. Proper lens alignment and sample placement are important because the measured signal depends strongly on system alignment and beam focusing on the device under test (DUT). After alignment, the system performance was characterized by beam focusing measurements, dynamic range analysis, and signal amplitude to establish a reliable experimental test bed.



Emitter	TPX50	TPX50	DUT	TPX50	TPX50	Detector
35 mm	70 mm	190 mm	245 mm	305 mm	400 mm	435 mm

Figure 3.3: Image and table of calibrated system according to Tera K15 manual for PCA and TPX50 lens alignment to achieve the best THz signal amplitude.

The most important calibration of the whole THz-TDS system was the optical lens and PCA alignment. The THz beam path was aligned in reference to the Menlo Systems Tera K15 calibration guidelines. Fig. 3.3 shows an image of the system's emitter, TPX50 lenses, and detector and the positioning along the 450 mm rail using the default reference locations provided in the system manual. These positions were measured accurately on the rails, with the emitter placed near 35 mm, the detector near 435 mm, and TPX50 lenses positioned according to the recommended optical path. The Menlo manual notes that these values can vary by approximately ±5 mm during alignment, so the listed positions were used as a starting basis for final calibration [19]. Minor iterative adjustments were made to the lens and antenna positions to maximize the measured THz pulse amplitude.

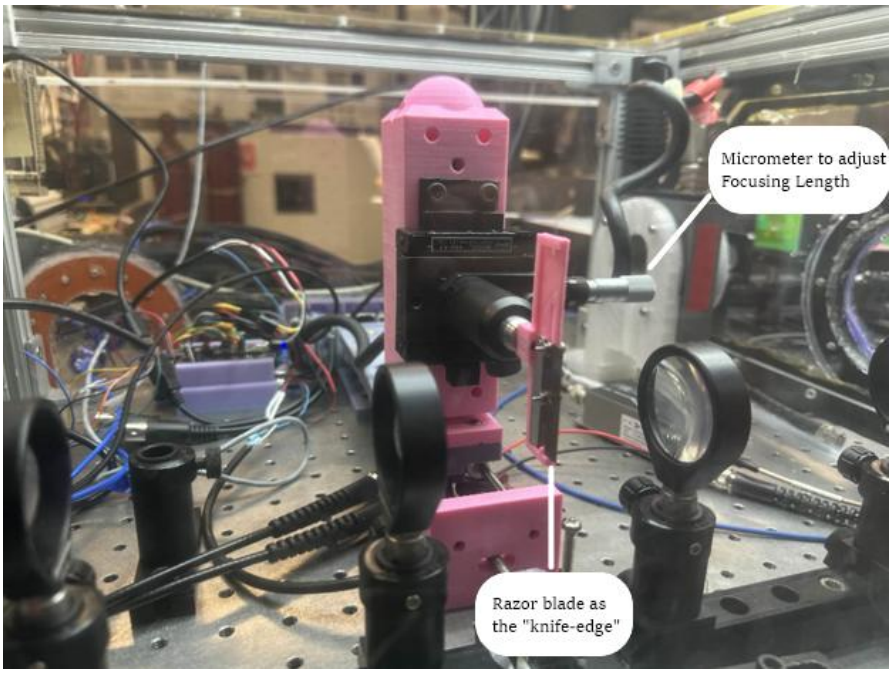


Figure 3.4: Experimental set-up for knife-edge experiment for the beam focusing characterization.

Before performing measurements on the sample, the position of the sample in between the two focusing lens is essential for experimentation in the THz-TDS system (Fig. 3.4). A focused beam allows for higher resolution measurements and imaging, and a stronger THz field at the sample plane.

The beam focusing was evaluated using a knife-edge measurement to locate the beam waist in the sample plane. In this measurement, a sharp edge is moved laterally through the beam path while the transmitted THz signal is measured at each iterative position. The change in signal as the knife-edge is swept the beam diameter can be reconstructed from the transmitted signals at each position. This approach is well known for Gaussian beam measurements and has also been applied to THz-TDS beam characterization, making it suitable for determining the focusing condition used in these systems measurements [20].

Assuming a Gaussian transverse beam profile, the THz beam intensity along the knife-edge scan direction can be written as:

$$I(x) = I_0 \exp\left(-\frac{2x^2}{w^2}\right). \tag{1}$$

Here, I_0 is the peak intensity at the center of the beam, x is the lateral position relative to the beam center, and w is the $1/e^2$ beam radius. This expression describes the spatial intensity distribution of the focused THz beam before it is partially blocked by the knife edge. During the knife-edge measurement, the blade is translated across the beam path and progressively blocks a larger portion of the THz beam. At each blade position, the recorded quantity was the peak-to-peak amplitude of the measured time-domain THz pulse. Since this measured signal is proportional to the portion of the beam that remains unblocked, the equation can be written as:

$$P(x) = \int_x^{\infty} I_0 \exp\left(-\frac{2u^2}{w^2}\right) du. \tag{2}$$

In this expression, $P(x)$ is the transmitted THz signal measured at knife-edge position x, with beam radius w, and u is the integration variable across the transverse beam profile. As the blade moves farther into the beam, the unblocked portion decreases, causing the measured THz signal to decrease. The Gaussian integral can be written using the error function and its complementary form:

$$\mathrm{erf}(z) = \frac{2}{\sqrt{\pi}} \int_0^z e^{-t^2}\, dt, \quad erfc(z) = 1 - \mathrm{erf}(z)\,. \tag{3}$$

These functions are used to express the knife-edge response in a closed form, allowing the measured curve to be fitted for the beam radius w. Using this relationship, the transmitted signal during the knife-edge scan can be written as:

$$P(x) = \frac{P_{tot}}{2}\left[1 - \mathrm{erf}\left(\frac{\sqrt{2}x}{w}\right)\right] \tag{4}$$

Here, P_{tot} is the total unblocked THz signal measured when the knife edge is fully outside the beam path. This expression was fitted to the measured knife-edge data, with w used as the fitting parameter that determines the beam radius. The total unblocked signal corresponds to the full integration of the Gaussian intensity profile:

$$P_{tot} = \iint_{-\infty}^{\infty} I(x,y)dxdy = I_0 \frac{\pi w^2}{2}. \tag{5}$$

After fitting the knife-edge response, the beam diameter was defined using the $1/e^2$ intensity convention as:

$$d_{beam} = 2w. \tag{6}$$

The measured knife-edge response and the fitted Gaussian-based curve are shown in Fig. 3.5.

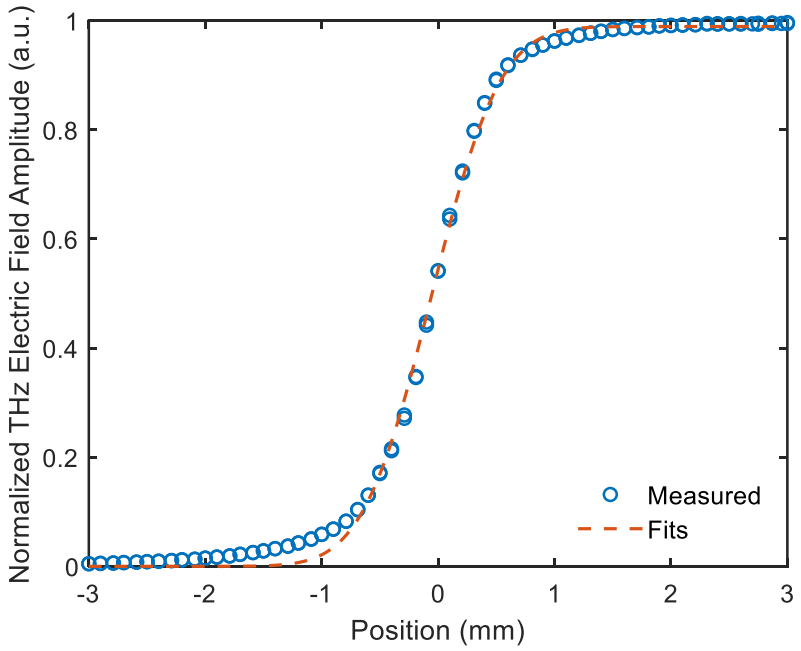


Figure 3.5: Measured THz signal during the knife-edge sweep, and the corresponding fitted Gaussian error function to determine the beam radius.

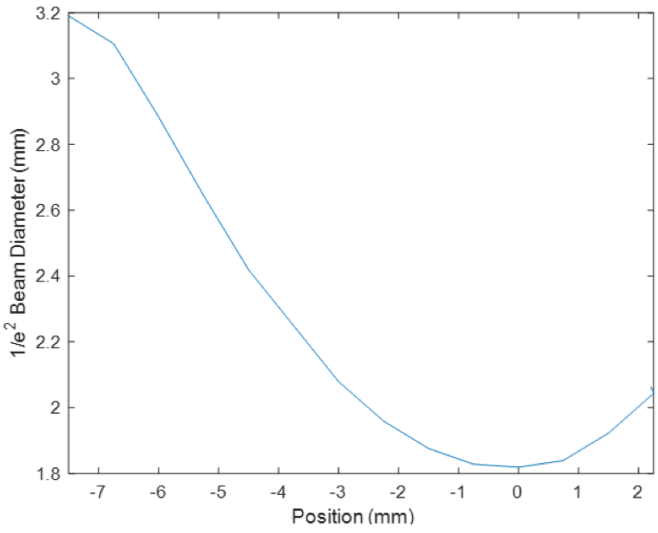


Figure 3.6: Resulting beam diameter versus relative focusing length of the knife-edge experiment.

During this experiment, knife-edge scans were performed at different focusing distances to determine the location of the beam waist. As shown in Fig. 3.6, the extracted THz beam diameter decreased as the focusing length was adjusted from approximately -7 mm to 2 mm, reaching a minimum beam diameter of ~1.8 mm. The lenses have an effective focal length of ~50 mm so the beam waist was expected to be ~50 mm which was normalized to 0 mm in these measurements. This trend shows that the THz beam waist occurred near 0 mm (50 mm), which was used as the optimal focusing positioning for the device during THz measurements.

3.2.4 THz-TDS System Characterization

After optical alignment the THz-TDS system was characterized to determine the operable frequency range for the THz-TDS measurements. This characterization was based on signal to noise ratio (SNR) and the dynamic range (DNR). This approach follows the method described by Neu and Schmuttenmaer, who used SNR, DNR, and a blocked beam noise measurement to evaluate the usable bandwidth of a THz-TDS spectrometer [18]. In this work, a reference purged

test was used as the signal baseline. The THz measurements were performed after a nitrogen purge of the measurement chamber to reduce unwanted signal attenuation and noise from atmospheric water vapor and oxygen molecules. To gather the system noise data, the beam path was blocked with a piece of metal. These measurements are the baseline for calculating SNR and DNR of the THz-TDS system.

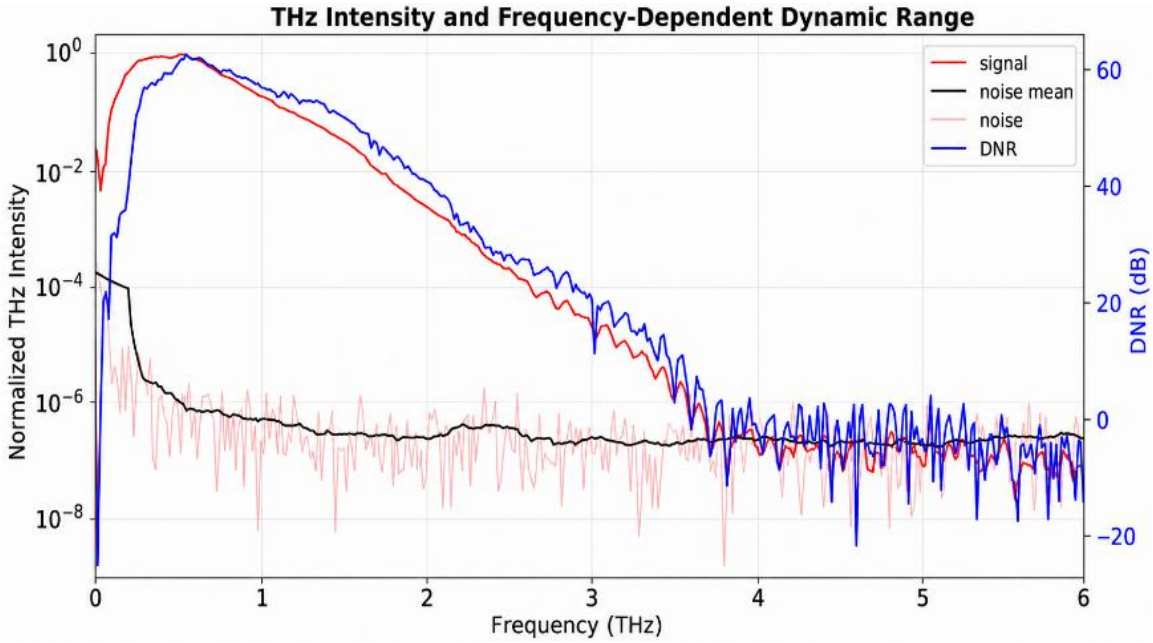


Figure 3.7: Measured purged THz signal intensity (red line) in comparison to the noise intensity (faded line). Noise mean (black line) smoothed with frequency domain filter; this data is used to find system DNR & SNR.

Figure 3.7 shows the normalized Fourier-transformed purged signal and the average noise floor. The purged spectrum reaches its maximum response below 1 THz and then gradually decreases with increasing frequency. At low frequencies, the purged signal is well above the noise floor, while above approximately 3.5–4 THz the signal approaches the noise level and is not reliable in measurement. The dynamic range of the system was calculated from the ratio of the purged signal spectrum to the average noise floor spectrum. The DNR reaches its strongest value in the low-frequency region, with values near 60 dB between roughly 0.4 and 1 THz. The dynamic

range then decreases as expected because the THz amplitude decreases with frequency while the noise floor remains relatively constant. The system remains above 20 dB until around 3 THz. This behavior indicates that measurements below 3THz are reliable giving an accurate baseline for measurements in the system.

The signal-to-noise ratio of the system was estimated by finding the ratio of the peak time-domain THz signal to the RMS of the system noise measurements. This calculation gave an SNR 65.8 dB; this indicates that the THz pulse is over 1000 times the system's time-domain noise. This high SNR ensures that the calibrated system provides a stable reference signal for detecting the desired tunable responses of the device. The SNR measurement confirms that the peak time-domain THz pulse is well above the measured noise level, and the DNR analysis is just as important because it shows how this signal quality changes with frequency, identifying the usable bandwidth where reliable data can be measured.

3.2.5 Thermally Tunable Response of STO: Terahertz

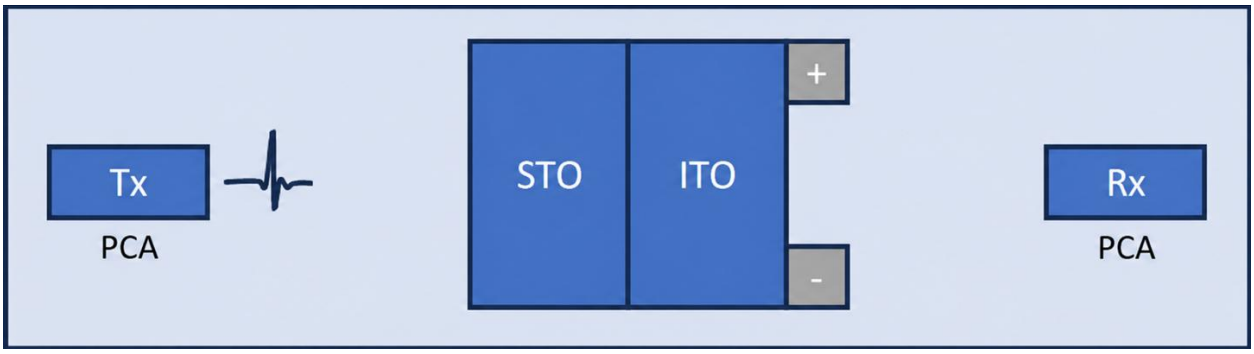


Figure 3.8: Simple diagram of THz measurements on STO/ITO sample (not to scale).

After calibrating and characterizing the THz-TDS system, the thermally biased ITO/STO sample was measured to evaluate whether heating produces a measurable change in the terahertz response of STO. To observe thermal tunability, the transmitted THz pulse was measured through the STO substrate at different applied bias conditions. The THz-TDS preserves the amplitude and

phase of the electric field, so changes in the measured time-domain waveform can be used to find changes in the material's refractive index.

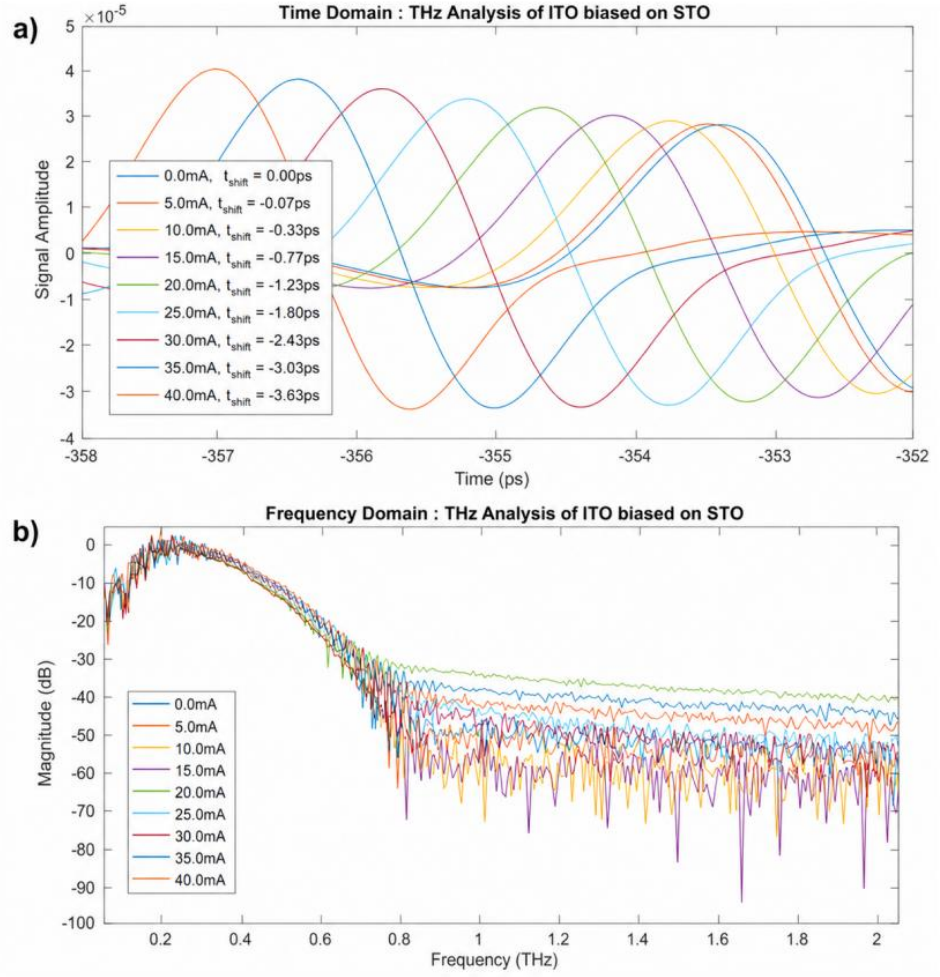


Figure 3.9: a) Measured time-domain THz pulse tunable response under increased applied biasing, b) Corresponding Fourier transform of time-domain measurements.

Fig. 3.9(a) shows the measured THz response of the biased STO sample. In the time domain, the main transmitted pulse shifts systematically with increasing bias, reaching a time delay of ~3.6 ps at the highest applied voltage. This time delay in the pulse shows that the propagation conditions of STO are varying as the sample is heated. Since the time delay of a transmitted THz pulse depends on the refractive index of the material, these results directly indicate a tunable THz response and allow for the derivation of the varying refractive index. The corresponding frequency

domain spectra was obtained by the Fourier transform of the measured time domain signals shown in Fig. 3.9(b).

To extract the refractive index, the measured sample waveform was compared to a reference waveform collected through the purged path. The time-domain reference and sample pulses were Fourier transformed to obtain $E_{DUT}(\omega)$ and $E_{REF}(\omega)$. The experimental transfer function was then calculated as $H(\omega) = E_{DUT}(\omega)/ E_{REF}(\omega)$. This transfer function contains the amplitude loss and phase delay introduced by the STO sample. A transfer-matrix model was then used to simulate propagation through the sample, including the thickness of the STO and the transmission response of the dielectric layer. The dielectric response was fit using a Lorentz oscillator model for the complex permittivity, and the model parameters were adjusted until the simulated response matched the measured transfer function and corresponding time-domain pulse. Once the complex permittivity was obtained, the refractive index was calculated from $\tilde{n}(\omega) = n(\omega) + i \cdot k(\omega)$ where $\tilde{n}(\omega) = \sqrt{\tilde{\varepsilon}(\omega)}$.

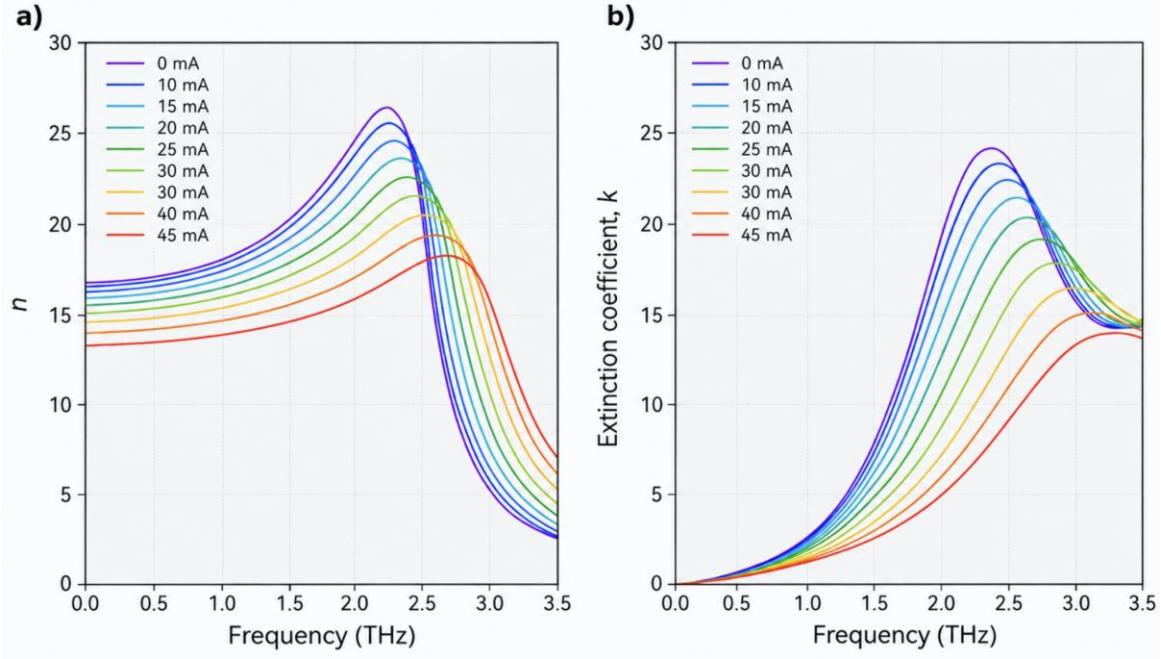


Figure 3.10: Extracted a) tunable refractive index and b) extinction coefficient of STO vias biasing from 0 mA to 45 mA.

Fig. 3.10 shows the extracted refractive index, n , and extinction coefficient, k, of the biased STO sample. The refractive index shows a clear thermally dependent shift; in the low frequency region of the THz system the refractive index decreases from ~15 at 0 mA to ~12 at 45 mA. An even larger change is observed near the refractive index peak around 2–3 THz, where the peak refractive index decreases from ~25 to below 17 as the applied biasing and temperature increases. The resonance peak also shifts toward higher frequency with increasing bias, indicating that the induced Joule heating results in tunable response of STO's dispersion. The extinction coefficient follows a similar trend, with the absorption feature decreasing in magnitude and shifting to higher frequency as current increases. Together, these results demonstrate that the applied thermal bias produces a strong modification of the STO THz response, affecting both the propagation delay and spectral absorption of the transmitted pulse.

These results represent the demonstration of THz tunability in this project. With only electrical bias applied to the ITO thin-film heating layer, STO produced a large and measurable

shift in the refractive index. This strong response is consistent with STO's low-frequency dielectric behavior, which is strongly influenced by temperature responsive polar phonon modes. This confirms that STO is a promising thermally tunable dielectric platform in the terahertz regime. At the same time, the extracted extinction coefficient shows that this tunability is accompanied by noticeable loss, which is important for future THz device consideration and material integration in THz systems. Although the sample is not yet an optimized THz component, these measurements show that the thermally controlled platform developed in Chapter 2 produces a significantly tunable device using STO.

3.3 Thermally Engineered STO: Infrared Response

3.3.1 Section Overview

In addition to the terahertz measurements discussed in chapter 3.2, the thermally induced optical response of STO was also investigated at infrared frequencies. The purpose of this section is to determine whether localized heating can produce a measurable and tunable change in the infrared reflectance response of the STO sample. This measurement provides a complementary frequency domain analysis on the thermally engineered behavior of STO and helps evaluate whether the dielectric response to sample temperature is observed in other frequency ranges also produces observable changes in the infrared regime.

The infrared response was characterized by using Fourier-transform infrared spectroscopy (FTIR) reflectivity measurements. Using the same ITO/STO device as the THz-TDS measurements, electrical bias was applied to the ITO heating layer to induce a temperature change across the STO substrate, and the reflected infrared signal was recorded as a function of bias condition. This recorded data of the reflectance at different applied currents allows analysis of how

the refractive index of STO varies with the induced Joule heating. This analysis is used to assess the extent of infrared tunability and to determine whether the response is similar to other frequency bands.

3.3.2 Literature Review: Infrared Response of STO

The optical response of STO is known to vary with temperature because its dielectric behavior is connected to lattice structure vibrations and optical phonon modes. In the infrared region, Dore *et al.* measured transmittance and reflectance of STO and extracted temperature dependent refractive index data over a broad infrared frequency range [21]. This study shows that STO has a measurable temperature dependent infrared optical response. Temperature dependent refractive index behavior of STO has also been studied in the visible and near IR regions. Toyoda and Yabe measured the refractive index of STO from 450 to 1600 nm from room temperature to 400 °C and showed that the thermal coefficient of refractive index depends on both wavelength and temperature [11]. This research observers a tunable refractive index, finding dn/dT varying from approximately $-7 \times 10^{-5}\,K^{-1}$ to $-1 \times 10^{-5}\,K^{-1}$. Toyoda and Yabe observed a stronger shift of refractive index at shorter wavelengths and lower temperature regions. This is explained by the thermal expansion of the material reducing the refractive index with rising temperature.

These prior studies establish the optical constants of STO are temperature dependent, but most of the research was performed by controlling the bulk sample temperature rather by localized Joule heating. Using current applied through the ITO layer to induce heating creates a practical method for modifying the optical response without changing the external measurement environment. This makes the FTIR measurement useful not only for observing STO's infrared response, but also for evaluating whether electrical heating can be used as a tuning mechanism at infrared wavelengths. Comparing the infrared measurements under different bias conditions help

determine whether the temperature dependent infrared properties reported in previous literature can translate into an experimentally observable tuning response in reflectivity measurements.

3.3.3 Infrared Measurements & Result Analysis

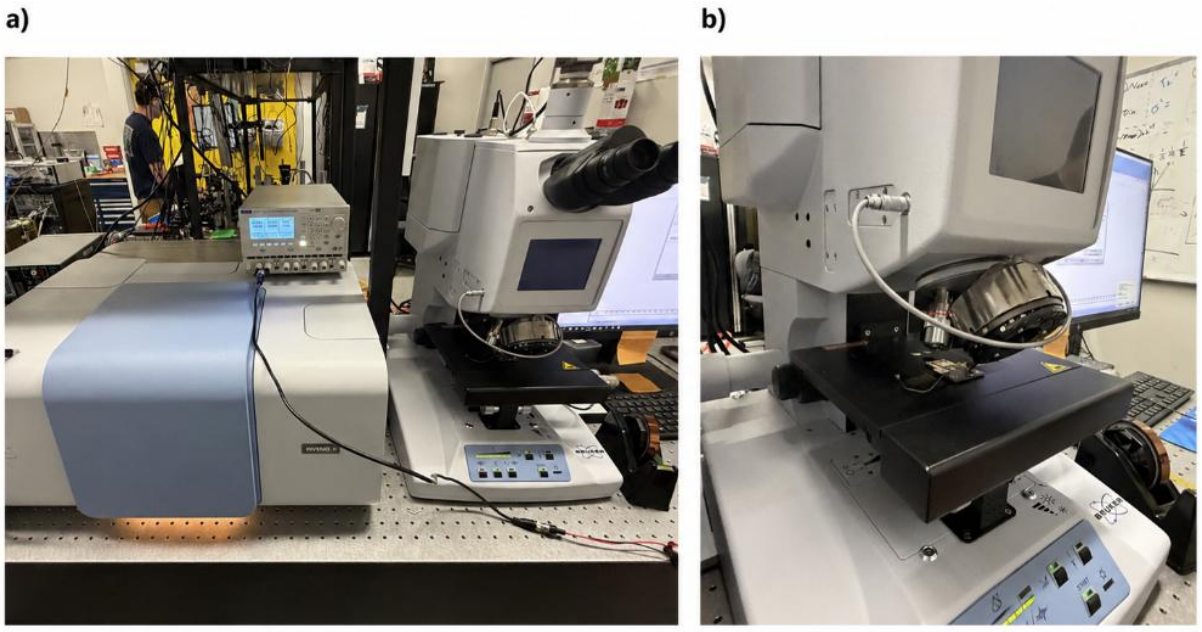


Figure 3.11: a) Experimental set up of FTIR system, b) Sample placement on FTIR during infrared measurements.

The FTIR system (Fig. 3.11) was used to evaluate the thermally induced response of the ITO/STO device at infrared frequencies. In these measurements, the FTIR was used in reflectance mode to analyze the infrared response of the thermally biased sample at different applied currents. The measurement results in Figure 3.12 show the superimposed infrared reflectivity of ITO/STO measured from approximately 1.5 μm to 17 μm, biasing the sample from 10 mA to 50 mA. From 1.5 μm to ~12 μm, the reflectivity follows a similar trend, and the thermally dependent change is relatively small. The Joule heating from ITO produces a minor downward shift in reflectivity even with large biasing steps. This shows that the thermally tunable response of STO is observable at infrared, but the tunable response is weaker in the shorter wavelength region of the FTIR

measurements. A much stronger tunable response is observed at the larger measured wavelengths, past approximately 13 µm. The reflectivity in this region increases sharply with wavelength, as current and temperature increases, the reflectivity slightly decreases and shifts toward longer wavelength. This tunable response is largest at 17 µm with reflectivity decreasing ~6% from 0 mA to 50 mA. These results show that the thermal response of ITO/STO is not uniform across the measured infrared spectrum but provides a more significant tunable response at the larger measured wavelengths.

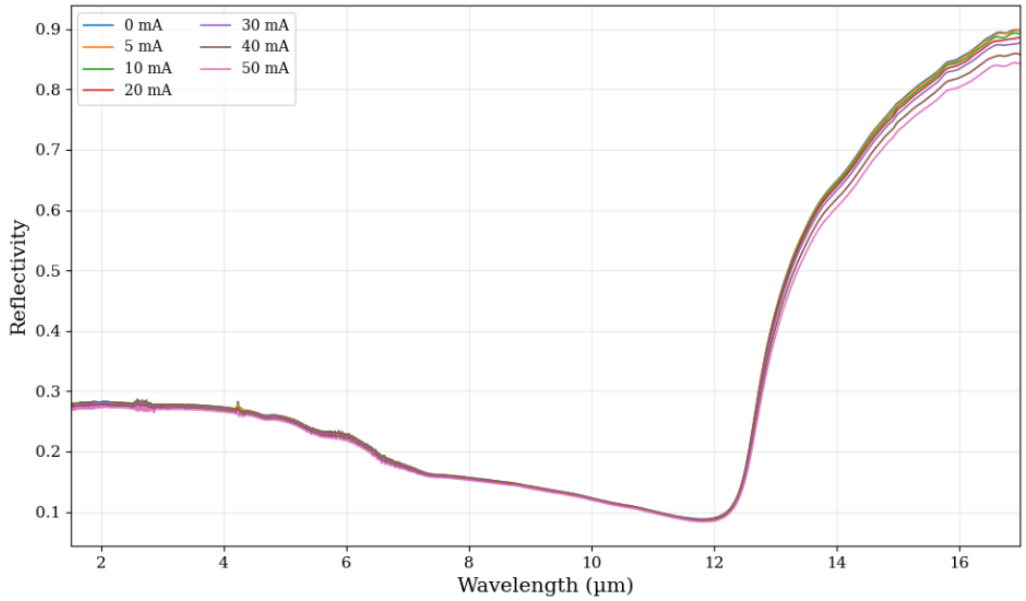


Figure 3.12: Measured reflectivity spectra from 1.5 µm to 17 µm under biasing from 0-50 mA

To observe the tunable sensitivity of the sample's refractive index behavior, the reflectivity can also be converted into an apparent refractive index using a simplified normal incidence Fresnel relation. This relation is under the approximation of negligible absorption; the apparent refractive index is estimated from the measured reflectivity as $n_{app} = (1 + \sqrt{R})/(1 - \sqrt{R})$. This value should not be interpreted as an accurate representation of the complex refractive index because STO is lossy and has infrared absorption. An accurate representation of the refractive index would require information such as ellipsometry, Kramers-Kronig analysis, and model fitting. The

calculated n_{app} is used only for qualitative analysis of how the induced thermal biasing causes shifts in the material's optical parameters.

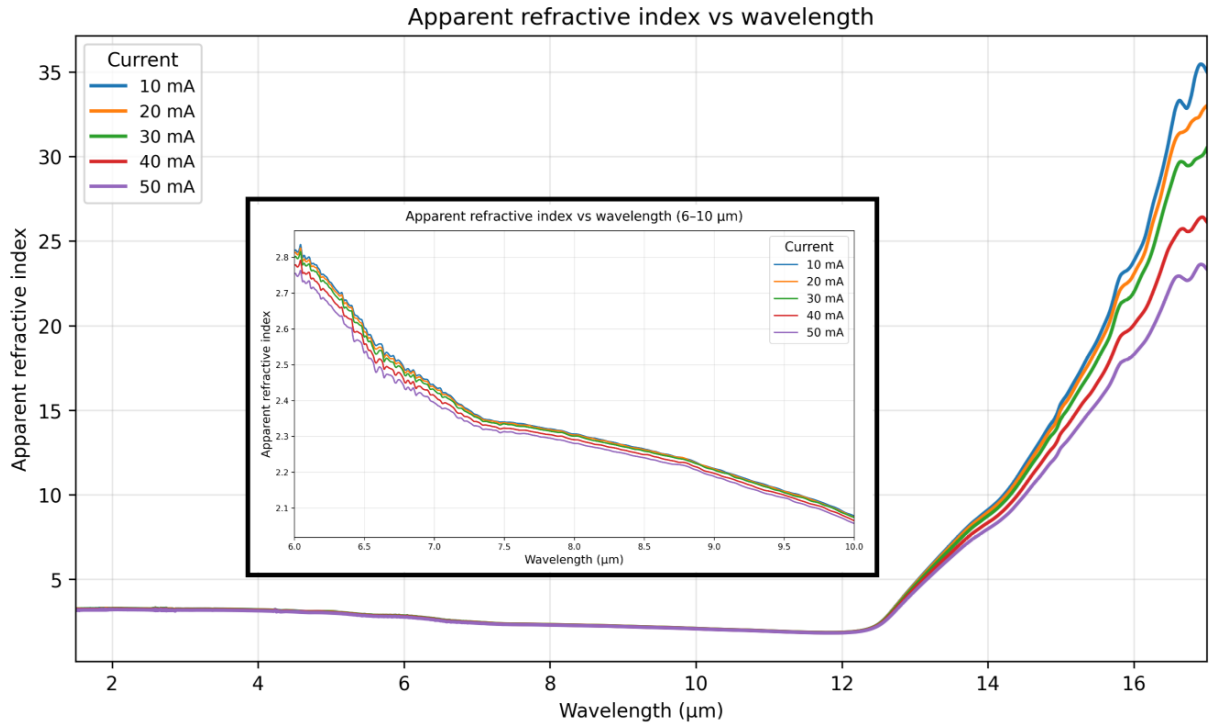


Figure 3.13: Calculated apparent refractive index vs wavelength from 1.5 μm to 17 μm under different bias conditions and zoomed plot from 6 μm to 10 μm

The plotted results of n_{app} are shown in Figure 3.13. From 1.5 μm to ~13 μm, the apparent refractive index remains low relative to the larger wavelengths, and the tunable response is small, this is consistent with the observations of the reflectance in this region and is expected because of the Fresnel relation used. The trends begin to separate much more past 13 μm as the apparent index and reflectance significantly increase with wavelength. Like the reflectance plots, the thermally induced response is much greater here, the decrease in the apparent refractive index agrees with the negative response to temperature in literature. As mentioned, large magnitudes past 13 μm should be interpreted carefully because this calculation is based only on reflectivity and does not fully account for absorption.

These FTIR results fit between the visible and THz behavior discussed in this chapter. In the visible and infrared region, STO shows only small thermally induced changes, while the THz measurements show a much larger refractive index shift. The stronger response in the FTIR reflectance suggests that the material becomes more sensitive as the measurement approaches phonon mode related behavior, but at the measured IR region the tunable response is not as direct or significant as in the THz regime, where STO's dielectric properties are more strongly influenced by polar phonon modes.

3.4 Summary

This chapter demonstrated the thermally controlled optical response of STO in the terahertz and infrared frequencies. The strongest tunability was seen during the THz measurements, with electrical bias applied to the ITO heating layer producing a clear and strong dielectric response. This verifies that thermally biased STO can strongly modify THz propagation, although the extinction coefficient shows that material loss must be considered in future applications. The FTIR measurements showed a weaker but measurable tunable response, with small changes at shorter wavelengths and larger response near the larger measured wavelengths. Compared with the THz response, the infrared tunability is less significant for practical device use because the measured changes are smaller and loss becomes more limited at these smaller wavelengths with a sample 0.5mm thick. The results of this chapter show how STO is promising as a thermally tunable platform in the THz regions, while the infrared measurements support the idea of temperature dependent optical parameters in STO.

4 Thermally Controlled Guided Device

4.1 Introduction & Overview

This chapter extends the analysis of a thermally tunable STO platform to the microwave region. Rather than measuring infrared or THz transmission through the substrate, a coplanar waveguide (CPW) was fabricated directly on the STO surface so that the RF signal propagates along a guided structure. The goal of this device is to observe if thermal biasing can produce a measurable change in the microwave response of STO up to 10 GHz. A 3 mm strip of ITO was used to induce heating, while fabricated gold CPW provided the path for RF signals. A major design challenge was the high permittivity of STO because it increased the waveguide capacitance and made a practical 50 Ω CPW design very difficult to implement onto the 10 mm × 10 mm sample.

In summary, this chapter follows the development of the STO RF device from the initial CPW design constraints to the final measurement platform. First, how the high permittivity of STO affected the waveguide geometry and why the final design required a practical compromise rather than a fully matched 50 Ω line will be explained. The chapter then connects this CPW design to the design of PCBs for the experimental analysis of the tunable response of STO at radio frequencies.

4.2 Coplanar waveguides on STO

4.2.1 High-Permittivity Substrate Design Considerations

For a low-loss transmission line, the characteristic impedance depends on the ratio of inductance to capacitance per unit length, $Z_o = \sqrt{L/C}$. The effective capacitance in a CPW is

influenced by the center conductor width, ground plane spacing, and the dielectric substrate under the trace. When using a high-permittivity substrate in a CPW design, the electric field energy is stored in the dielectric, this increases the capacitance per unit length of the waveguide. This directly decreases the characteristic impedance and slows the propagation velocity, $v_p = 1/\sqrt{L'C'}$. This is very important for STO-based CPW devices, where the large dielectric constant of STO, ~300 at RF, makes practical transmission line geometries have a characteristic impedance well below 50 Ω [22].

Strontium titanate is difficult to work with because its microwave permittivity is much larger than typical RF substrates. Bulk STO has been reported to have a room temperature permittivity of ~300, which is far above common dielectric substrate such as FR-4 or Rogers materials, which range from 4-10 [9]. This forces the CPW impedance significantly below 50 Ω for practical device dimensions. This was a very difficult design constraint for 50 Ω matching but does not remove the ability to observe a tunable response with this device.

This challenge has been discussed in recent work on STO related CPW transmission lines. Santavicca *et al.* demonstrated approximately 50 Ω CPW transmission lines using superconducting niobium nitride (NbN) nanowires on a bilayer substrate consisting of a 100 nm STO film on high-resistivity silicon [22]. In this work, thin-film STO on silicon was important because the effective permittivity could be controlled by the CPW dimensions. The small nanoscale structures interacted strongly with the thin STO layer, while wider structures interacted more with the silicon substrate. The authors noted that while STO's high permittivity helps reduce the impedance of nanoscale NbN transmission lines toward 50 Ω, wider macroscale transmission lines on STO are driven well below 50 Ω because the kinetic inductance of the wires decreases while the capacitance remains high [22].

What makes this project much more difficult is that the CPW is fabricated directly on a 500 μm thick bulk STO sample rather than on a STO thin film supported by silicon paired with NbN nanowires. This causes the guided mode to interact strongly with the high-permittivity STO substrate. This makes it almost impossible to design the CPW dimensions to 50 Ω while also satisfying given design constraints for fabrication in the Center for Nano-MicroManufacturing (CNM2) at UC Davis. There were also additional design constraints for 1 mil (25.4 μm) gold wire bonding available at UC Davis's CNM2 present which made this design limit close to 25 Ω. Once the high-permittivity design considerations and fabrication limits were established, the designed CPW geometry was then refined through analytical estimates and repeated high frequency structure simulator (HFSS) simulations described in the following section.

4.2.2 CPW Design Geometry Optimization

The next step in this project was to design the CPW geometry for the guided wave device. The original goal was to design a 50 Ω transmission line so that the sample could be well matched for the Vector Network Analyzer (VNA) experiments. The large permittivity of the STO substrate made this challenging given the available design constraints. As mentioned previously, increasing the substrate permittivity increases the capacitance per unit length, which lowers the characteristic impedance of the transmission line. The effect of CPW geometry variables on the characteristic impedance can be understood from the conformal mapping description of coplanar waveguides. In a simplified CPW model, the characteristic impedance (Z_o) and the capacitance per unit length (C') relies on the elliptic-integral ratio $K(k')/K(k)$, where the factor is k defined as $k = W/(W + 2G)$. In this equation, W is the center conductor width and G is the gap between the center conductor and the coplanar ground planes. This relationship shows that decreasing the center conductor width increases inductance and increasing the ground spacing decreases the line

capacitance and results in a larger characteristic impedance. Varying these design parameters can raise the impedance, but the high dielectric constant on STO and finite sample size limits how much the CPW impedance can be increased with these parameters [23].

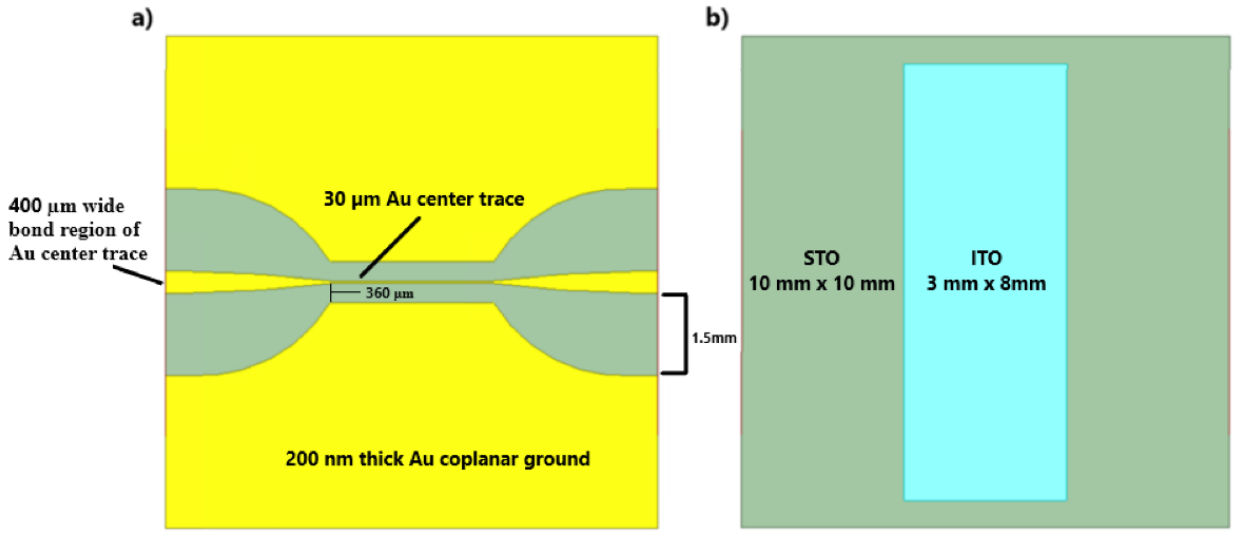


Figure 4.1: a) Top view HFSS model of the Au coplanar waveguide on STO, b) rear view of CPW sample with 3 mm wide ITO strip (light blue).

A 0.4 mm CPW pad width was selected at the outer regions of the device to provide reliable access for multiple 1 mil gold wire bonds [22]. This pad size was important for practical assembly, but it also created a low-impedance section because the wider conductor strongly increased the capacitance between the center trace, coplanar grounds, and high-permittivity STO substrate. Prior to selecting the ground spacing for this section of the CPW, preliminary LineCalc estimates were performed for the conductor backed region using the same pad width. These estimates showed that, within the size constraints of the 10 mm × 10 mm STO sample, the theoretical impedance could not be increased above approximately 11 Ω with a 0.4 mm trace because the required ground spacing would extend beyond the practical device area. To increase the impedance toward a more usable value, the width of the center conductor in the center region was narrowed significantly. Therefore, a 30 µm center conductor width was selected as a practical compromise, producing a

design near a region of 25 Ω. Beyond this point, increasing the ground spacing provided only limited improvement because the sample size constrained the available gap, while the backside ITO layer maintained strong capacitive coupling through STO. This limitation was much less in the outer sample regions, where the CPW is not conductor backed by the ITO layer and the fields were primarily controlled by the coplanar grounds and the center conductor width.

The backside ITO layer also meant that the CPW could not be modeled as a uniform transmission line across the entire sample. Based on preliminary LineCalc calculations, a 3 mm wide ITO strip was selected for the center of the device so that thermal biasing could still be done without placing a conductive layer beneath the full CPW structure. If a larger ITO region like the THz devices were used, the CPW would behave more strongly as a conductor backed waveguide over a larger area, this restricts the impedance significantly. The preliminary estimates showed that even with the available ground spacing on the sample, a fully conductor backed geometry would remain below approximately 12 Ω with the size needs of the bonding pads. To compromise, the ITO was limited to the center region, and the transition from the unbacked CPW sections to the partially conductor backed region was optimized in HFSS.

The transition from the 0.4 mm wire bond pad to the 30 μm CPW center trace was also an important part of the design. A direct step between these two widths would introduce a strong impedance discontinuity, so a tapered trace was used. Several taper configurations were evaluated in HFSS, including a linear taper, concave taper, and convex taper for the coplanar ground. The use of concave and linear tapering on the ground planes improved transmission, but the response improved best when the ground plane was shaped with an inverted taper around the tapered signal trace. Once this was determined, the taper depth was iterated through simulation to optimize performance.

Figure 4.1 shows the final CPW layout selected for the STO guided wave device. This design should be viewed as a first rendition structure rather than a fully optimized transmission line. The main goal was to create a measurable RF path through the STO sample while still allowing thermal biasing through the backside ITO layer. Because of the constraints of fabrication, wire bonding, sample size, and project time constraints, accepting an impedance closer to 25 Ω was necessary to preserve device manufacturability and evaluate whether thermally induced microwave tunability could be observed.

4.2.3 Finalized Design Simulation Results

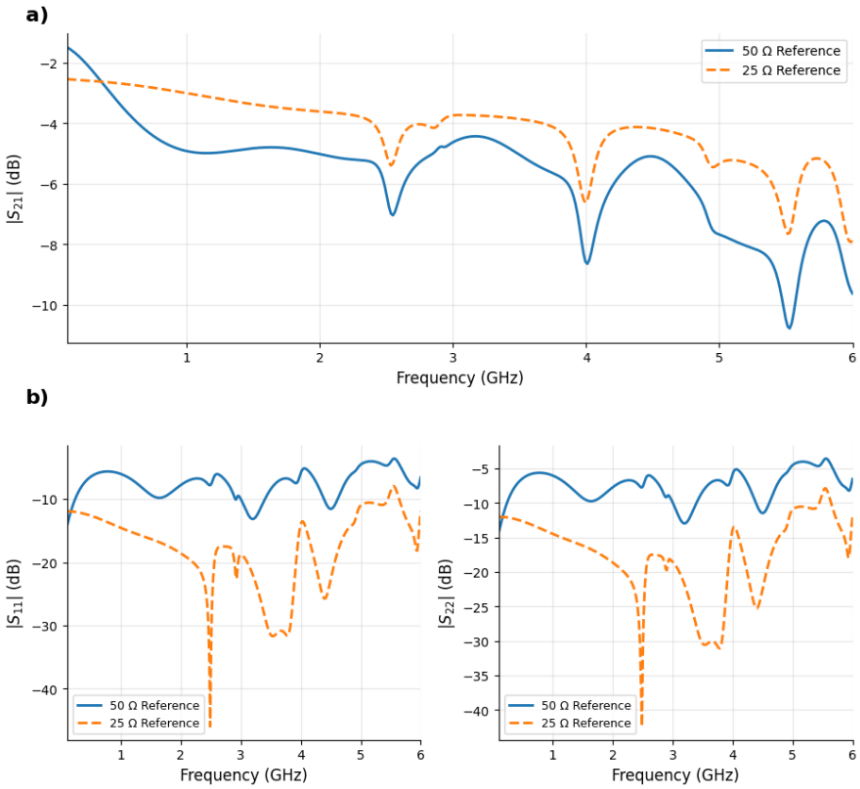


Figure 4.2: Simulated S-parameters of CPW STO design, a) S21 (transmission) & b) S11 and S22 (reflection).

The finalized STO CPW geometry was simulated to evaluate the expected RF response prior to tape out and fabrication. As mentioned in section 4.2.2, the design impedance was closer

to 25 Ω, the simulated S-parameters were plotted by changing the wave port to a 25 Ω and a 50 Ω reference to compare the finalized design with the conditions of the VNA experiments. Figure 4.2 shows the simulated transmission and reflection response of the final design. The transmission of the design, (S21) in Fig. 4.2a shows a gradual linear decrease in S21 across the band, with several resonant dips likely caused by impedance discontinuities and the coupling through the high-permittivity substrate. Although the response doesn't meet the criteria for a low-loss transmission line, it remains continuous and measurable across the simulated frequency range, which was sufficient for the first iteration of this device. The reflection responses in Fig. 4.2b show that the 25 Ω reference produces lower reflection than the 50 Ω reference, this is as expected given the lower impedance design considerations and constraints. These simulations were used as a baseline confirmation of a measurable RF path prior to device fabrication and experimental measurements to observe the significance of the thermally tunable response in the microwave frequency region.

4.3 Device Fabrication

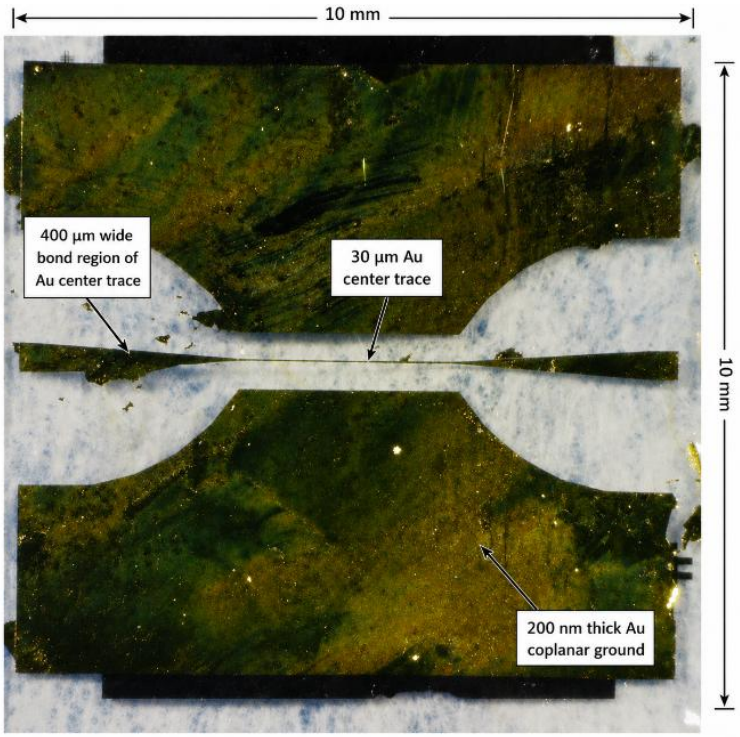


Figure 4.3: Fabricated coplanar waveguide STO sample.

As with the ITO/STO samples described in Section 2.4, the RF CPW sample fabrication was carried out at CNM2 by a project collaborator. The CPW device followed the same general lithography, metal deposition, and lift-off approach, but there needed to be additional steps because the sample used a double-sided structure. In this sample, the ITO heating layer was patterned on one side of the STO substrate, while the gold CPW waveguide was fabricated on the opposite side.

The double-sided process introduced handling challenges because the completed ITO channel had to be protected while the CPW was patterned on the opposite surface. The CPW features included microscale geometries which required reliable and accurate photoresist deposition. To improve the lithography process, the CPW pattern was written using a Raith PicoMaster 200 UV laser writer with MICROPOSIT S1813 positive photoresist.

After lithography, the CPW metal layer was deposited using the same titanium and gold approach described previously. A thin titanium layer was used for adhesion to STO, followed by a thicker gold layer to form the RF conductor. The finalized RF sample consisted of a backside ITO heating structure and the designed gold CPW structure. The double-sided sample introduced challenges in fabrication but was essential to simultaneously bias the sample thermally and have a RF signal path across the sample. allowed electrical biasing of the ITO layer to thermally tune the STO while the RF signal propagated along the CPW on the opposite surface.

4.4 PCB Prototyping

4.4.1 Sample PCB Design Requirements

After the STO CPW sample was designed, a separate PCB interface was required because the CPW pads on the STO chip were too small to access with standard connectors or probes. The PCB served as an intermediate platform between the VNA measurement setup and the STO device, providing RF access, mechanical support, and thermal tunability using ITO biasing.

The PCB layout had to support both the RF CPW measurement and the thermal tuning mechanism. Like previous PCB designs mentioned in Chapter 2, a square cut out in the center of the board was required so the sample could be mounted over an open region, while the resting copper contact areas provided heat dissipation and sample support. This implementation was essential because the ITO strip is located on the opposite side of the STO sample from the gold CPW design. Bonding pads needed to be placed near the cutout on the back of the PCB to allow the backside ITO strip to be biased without interfering with the top of the sample.

RF access to the sample was achieved using copper CPW feedlines with an ENIG (Electroless Nickel Immersion Gold) surface finish, the immersion gold layer allows for reliable

wire bonding from the experimental board to the sample. The PCB also included a straight CPW through line and a wire bond CPW test structure, these traces are important for analyzing the feedline's impact on the measured S-parameters. In the PCB design, copper was intentionally removed beneath the RF port region of the STO sample to reduce unwanted ground coupling across the signal path. These requirements guided the PCB CPW feedline design and test-structure layout described in the next section.

4.4.2 PCB CPW Feedline Design & Simulation

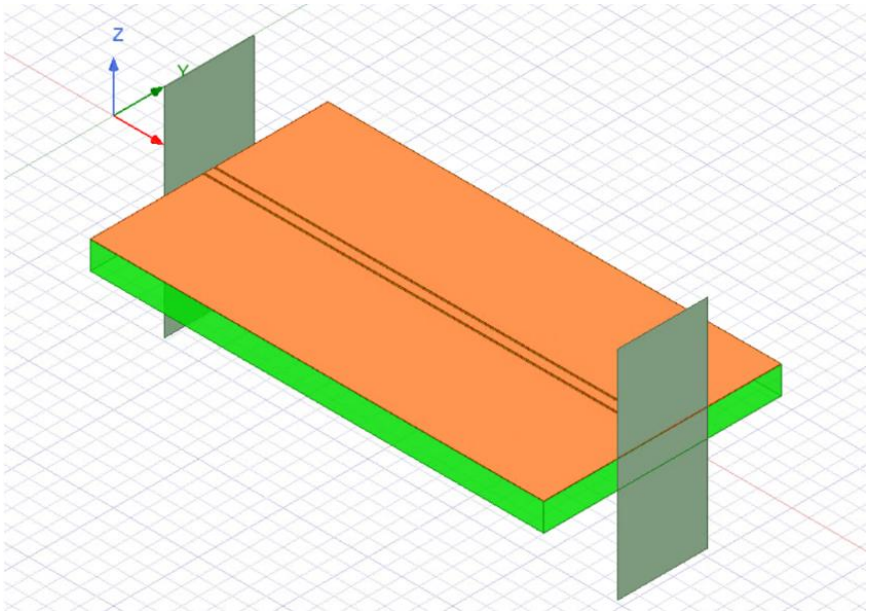


Figure 4.4: HFSS 3D model of PCB CPW design, the orange material is copper, and the green material represent the FR-4 Substrate.

Before designing the PCB, the RF feedlines to access the sample had to be designed and characterized to provide a reliable measurement path from VNA to the device. The known parameters of the PCB were set by board stack up and the PCB manufacture specifications. These essential parameters were 1.6 mm FR-4 substrate thickness, an FR-4 relative permittivity of ~4.4, and copper thickness of 1.4 mil (0.036 mm), these parameters were necessary for calculating the CPW geometry.

The trace width of the CPW was chosen based on the selected SMA edge-launch connector footprint, 0.54 mm. Rather than designing a narrow 50 Ω trace and tapering it into the SMA pad, the PCB CPW center conductor was sized to match the SMA signal pad width to avoid unwanted impedance discontinuities in the SMA launch regions. This reduced the need to taper the trace or apply ground spacing adjustments. This design choice was guided by practical RF PCB layout considerations discussed in an Altium edge-launch SMA design article, where the SMA edge connector transition is modified using trace tapering and ground spacing adjustment to fix impedance discontinuities at launch [24].

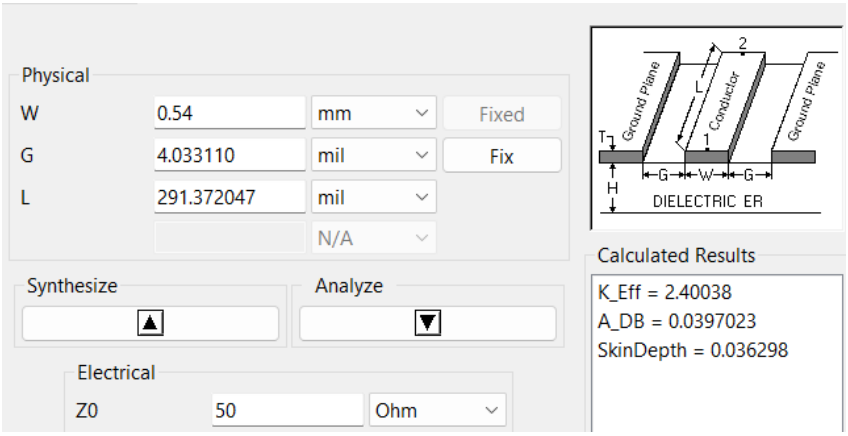


Figure 4.5: Calculated coplanar waveguide parameters using Keysight ADS LineCalc tool.

Once the PCB CPW trace width was selected to be 0.54 mm, there remained no more unknowns needed to calculate the ground spacing needed to achieve a 50 Ω on the PCB substrate. Using the parameters mentioned and the Keysight ADS LineCalc tool (Fig 4.5) the conductor trace must have a ground spacing of 4 mil (0.1 mm) from each edge to achieve a 50 Ω impedance profile. After selecting all design parameters, the resulting CPW geometry was modeled in HFSS, as shown in Fig 4.2. This HFSS model was simulated using modal wave ports and an interpolating frequency sweep up to 10 GHz, this analysis was done to observe the CPW frequency response using the selected design parameters.

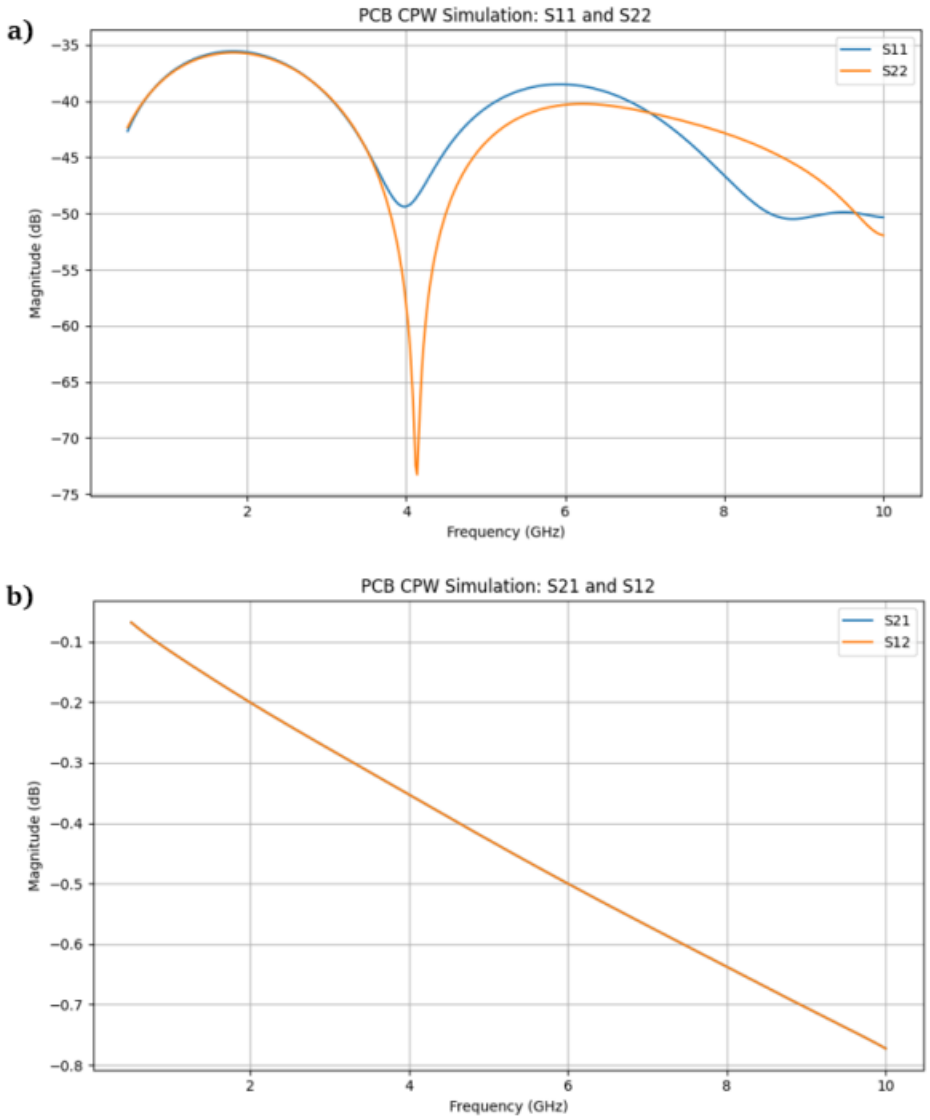


Figure 4.6: a) Simulated input reflection coefficient (S11) & output reflection coefficient (S22) of PCB CPW design, b) Simulated forward transmission coefficient (S21) & reverse transmission coefficient (S12) of PCB CPW design.

The simulated S-parameters were then found using this CPW design. In this simulation, the input and output reflection coefficients (S11 and S22), as well as the forward and reverse transmission coefficients (S21 and S22) are found to evaluate waveguide performance. S11 and S22 of the CPW are very well matched, maintaining below -35 dB across the frequency band (Fig 4.6a). For example, -35 dB means ~0.03% of power is reflected, this means the geometry of the CPW is matched well to 50 Ω. Fig. 4.6(b) displays the S21 and S12 of this CPW design, the linear

loss with frequency observed is consistent with the expected loss behavior of FR-4 at GHz frequencies. Djordjević *et al.* characterized FR-4 up to 12 GHz and reported that its loss tangent is approximately 0.02 and is relatively constant through the measured microwave band [25]. These simulation results established confidence in the geometry to use for the CPW feedline design on the PCB for this project and gave the confirmation needed to proceed with the PCB design.

4.4.3 Final PCB Layout

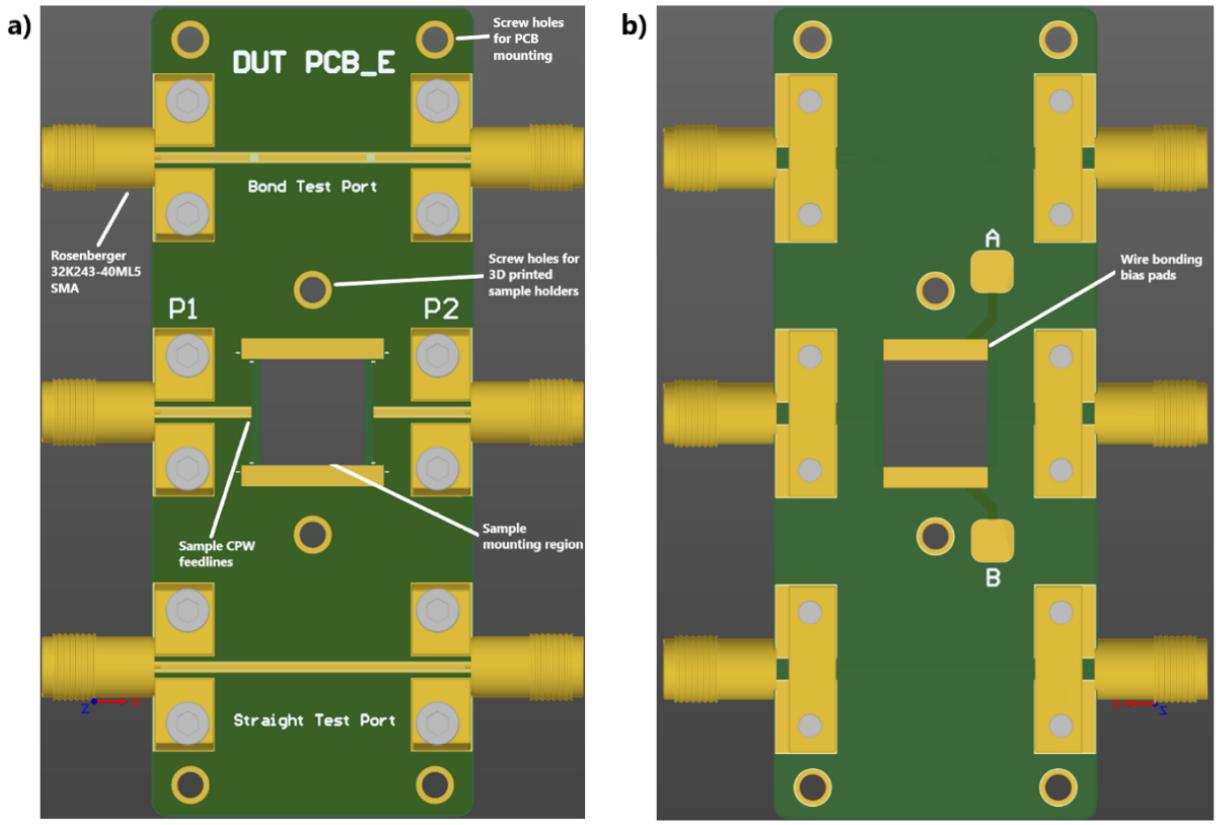


Figure 4.7: Final PCB layout for the fabricated guided device. a) Front view of PCB design, b) back view of PCB design.

The final PCB layout was designed to implement the RF, thermal, and measurement requirements discussed in Sections 4.4.1 and 4.4.2. The completed layout included the central sample cutout, copper contact regions for heat dissipation, CPW feedlines for RF sample access, backside bias pads for the ITO heating strip, and additional CPW test structures for fixture

characterization. Fig. 4.7 shows the full PCB design used for the guided-wave measurements. The feedline path was routed from the SMA launches toward the central cutout, where the PCB feedlines will be wire bonded to the fabricated device. As mentioned previously, additional traces were included on the same board to support later fixture anaylsis. The straight CPW through line was used to evaluate the performance of the baseline PCB feedline response, while the wirebond CPW structure was designed to evaluate the effect of the wirebond transition. For accuracy, the spacing for the gold wire bonding was designed to match the approximate wire bond length to the sample.

The choice of SMA connector was also important because the SMA launch is a significant factor in the performance of the measured RF response. The Rosenberger 32K243-40ML5 SMA connector was selected because of its small signal pin which can significantly helpreduce impedance discontinuities between the SMA pad and the CPW feedline. Additionally, the SMA uses screw-mounted ground contact, providing a mechanically secure connection to the PCB ground pads and improving connection reliability for repeatable experimental tests. Together, the final PCB layout provides this project with the essential requirements needed to effectively measure the thermally tunable effects on microwave frequencies.

4.5 Experimental Characterization of Device

4.5.1 Experimental Setup

The measurements of this device were performed using an Anritsu MS46122A VNA. The VNA was used to measure the two-port S-parameters of the device and observe the tunable response of these parameters under thermal bias. The measured frequency range was swept from 0.1 GHz to 6 GHz with 16,001 frequency points to provide high measurement resolution across

the band. To reduce noise during measurements an intermediate frequency bandwidth of 1 kHz was set.

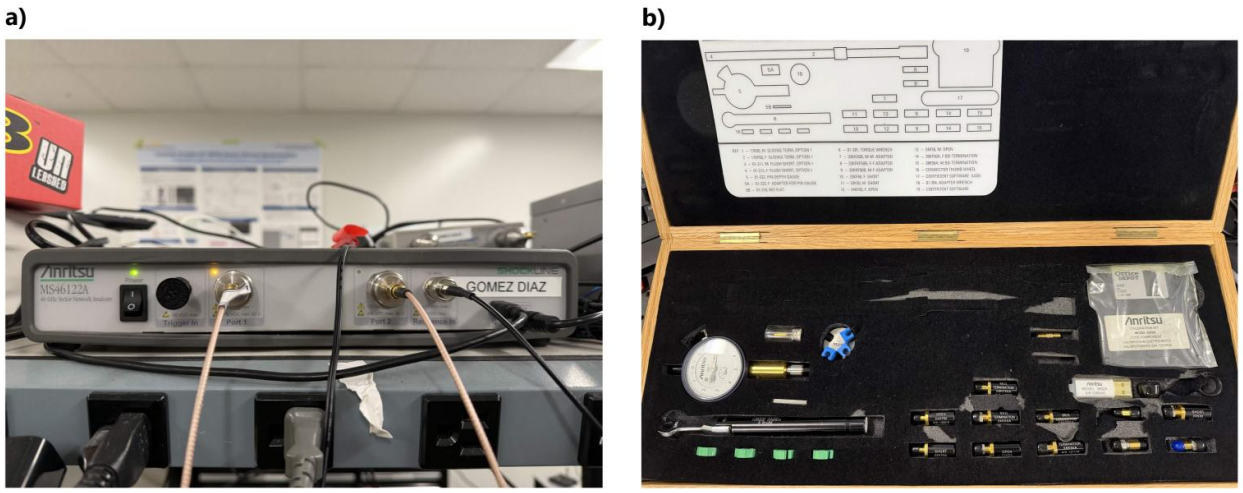


Figure 4.8: a) Anritsu MS46122A vector network analyzer used for RF measurements, b) SOLT calibration kit used for experimental set-up

Prior to measuring the device, it is essential that the VNA must be calibrated using a SOLT calibration procedure. The calibration used short, open, load, and through standards to establish the measurement reference planes. Fig. 4.8 shows the Anritsu VNA and calibration kit used for this experiment. After calibration, it is important that the same cable and connector positions are used to avoid change in calibration reference, to avoid measurement inaccuracies and increased insertion loss. A solution to avoid these inaccuracies was a custom 3D-printed measurement platform that was designed to improve repeatability during the VNA measurements. The platform was mounted directly to the optical table to establish a fixed position for the SMA ports during calibration and device measurements. This was important as it established an experimental platform for the board and allowing for consistent measurements.

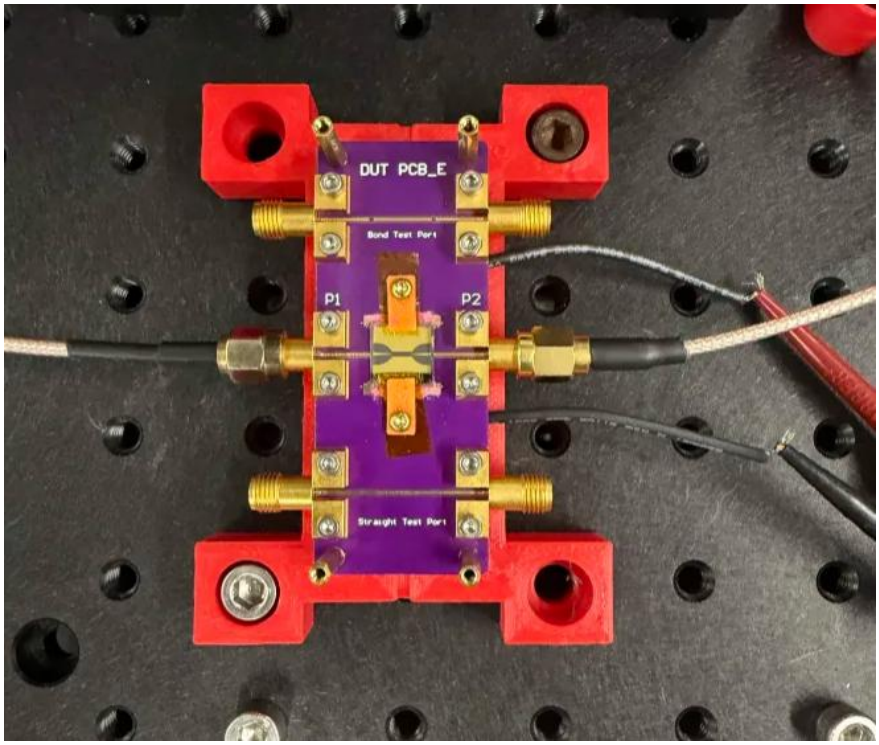


Figure 4.9: ITO/STO device during VNA measurements mounted in custom 3D-printed PCB holder.

Fig. 4.9 shows the device under measurement mounted in the 3D-printed platform. In this figure, the sample is being fixed in place using custom 3D printed tabs that apply pressure to the sample. This fixture is important, as any shifts in the sample's position can easily break wire bonds. This allowed the device to remain physically stable throughout calibration and repeated S-parameter measurements.

4.5.2 Device S-Parameter Measurements

Once the experimental setup was complete, the STO CPW device and PCB test structures were measured. These baseline measurements were used to characterize the RF response of the device before applying thermal bias to the ITO heating layer. Going into these measurements, the device was not expected to behave as a low loss transmission line. As discussed in Section 4.2, the high permittivity of STO and the fabrication constraints resulted in the finalized design to ~25 Ω.

The device was measured using a standard 50 Ω VNA system, an impedance mismatch was expected at both the input and output sides of the CPW. For an ideal transition between 50 Ω and 25 Ω, the reflection coefficient is given by $\Gamma = (Z_L - Z_0)/(Z_L + Z_0)$ which gives $\Gamma \cong 0.33$, which corresponds to ~11% reflected power at each port of the device. This is important when interpreting the S-parameters, since reduced transmission and increased reflection are expected from the design mismatch, even before considering dielectric loss, wire bond transitions, SMA transitions, and fabrication tolerance non-idealities. Despite these non-idealities, the goal is to observe tunable response of these parameters under induced thermal biasing.

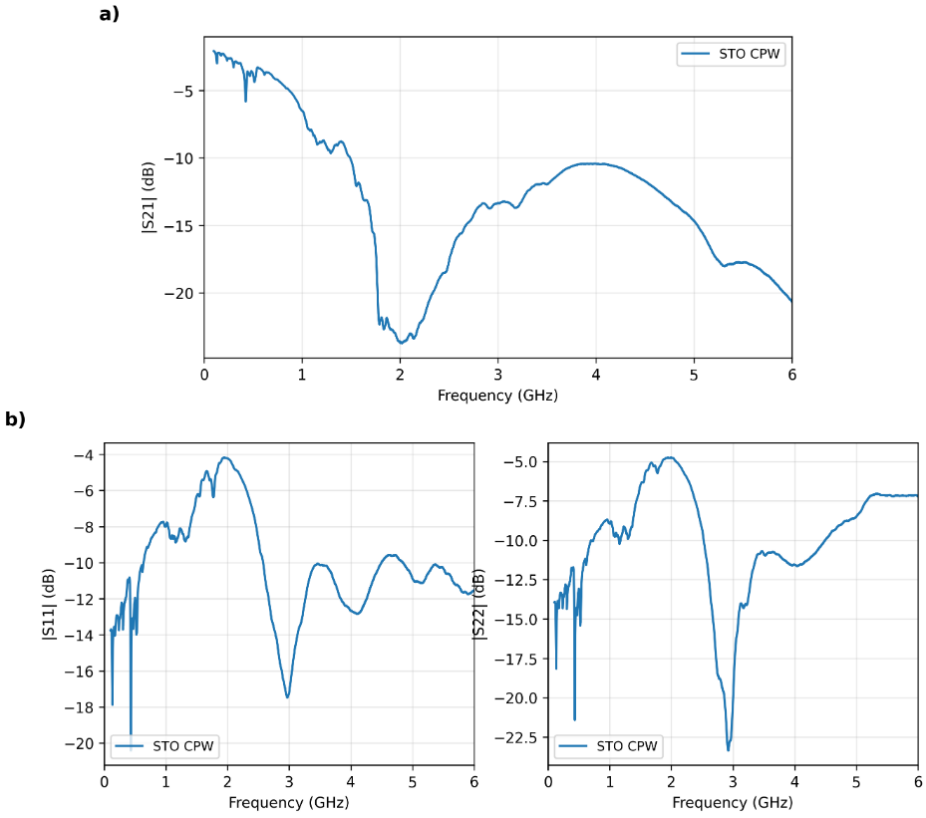


Figure 4.10: STO CPW device measurements under no induced thermal bias S-parameters, a) S21 (transmission) & b) S11 and S22 (reflection).

Figure 4.10 shows the measured baseline response of the fabricated device prior to any thermal biasing. The measured response includes the full integrated RF path from the PCB to the fabricated sample. As mentioned in previous sections, the device was designed near 25 Ω and

measured in a 50 Ω system, so the baseline response is expected to include both reflection and insertion loss from impedance mismatch. S21 has significantly more loss than the HFSS simulations, this is likely due to introduced loss from wire bonding, PCB loss, and SMA transitions to the feedline, but a clear RF path is functional to measure the tunable response. S11 and S22 ideally should be the same, but due to the same non-idealities there is minor variation in the response. The measured S21 response also contains a pronounced notch resonance near 2 GHz, which has the potential to provide a useful feature for evaluating the tunable response.

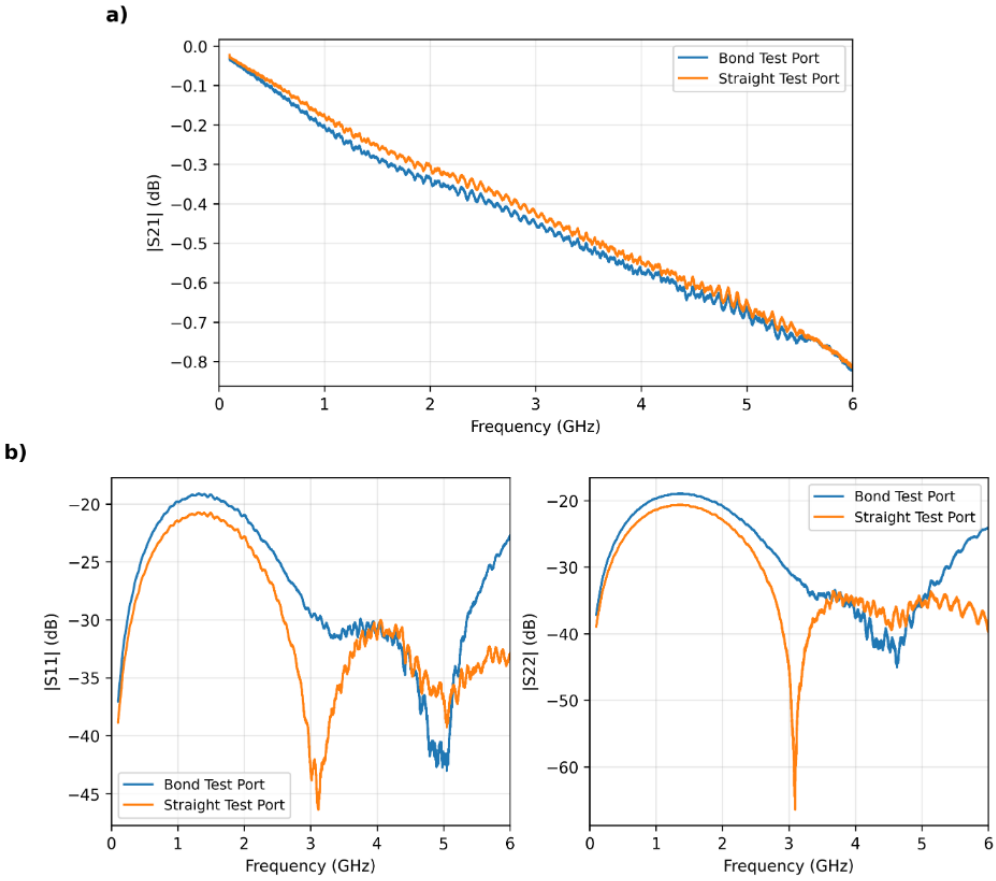


Figure 4.11: a) S21 (transmission) of the straight and wire bonded test ports, b) measured S11 and S22 (reflection) of the straight and wire bonded test ports

Figure 4.11 shows the measured response of the straight PCB CPW through line and the wire-bond CPW test structure. The straight CPW through line behaved as expected for an FR-4

feedline, showing an expected linear decrease in transmission across the measured band with minor oscillations due to VNA system noise. The wire bonded CPW test structure introduced minor non-idealities because the RF path includes the wire bond transitions, but the linear trend of the transmission remains close with the reflection parameters deviating at higher frequencies because of the increasing inductance of the gold wire bonds. The response of these test traces is as expected with non-idealities compared to previous simulation results because of the included SMA launch, PCB manufacturing, and wire bonding.

The test structures were used to support the analysis of the STO CPW measurements. Fixture de-embedding was investigated and originally the plan, but the mathematical correction introduced nonphysical artifacts in the S-parameters that are inconsistent with an expected passive device response. For this reason, de-embedded data were not used as the primary result. Instead, each bias condition was measured with the same calibration, cable positioning, and PCB fixture, so changes between bias states can still be used to evaluate the thermally induced RF response in the next section.

4.5.3 Bias-Dependent Tunable Response

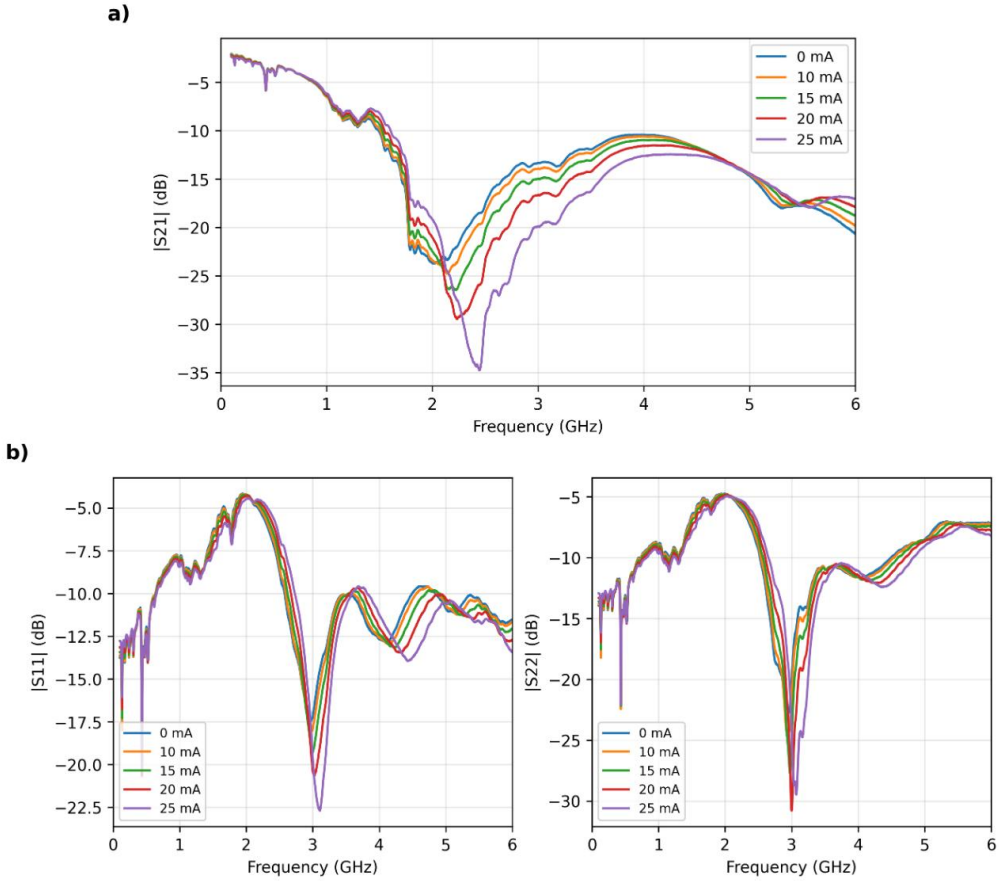


Figure 4.12: a) Measured S-parameters from 0 mA to 25 mA biasing on the back side ITO heating film.

After the unbiased response of the device was measured, current was applied to the ITO heating layer to determine the magnitude of tunable response at RF. Figure 4.12 shows the measured tunable response of the S-parameters. The most significant tunable response is observed around 2-4 GHz, where the notch resonance experiences a significant shift in frequency. S21 shows the transmission minimum near 2 GHz shifts by ~0.5 GHz across the measured bias range. This shift is consistent with a change permittivity of the STO substrate. As the ITO layer heats the sample, it is causing a shift in permittivity across the sample, which directly affects the capacitance per unit length of the CPW structure. Since the measured response contains resonance features across the measured band, a thermally induced change in the STO permittivity shifts the frequency

location of these features. These results show potential in this substrate for tunable resonator behavior from just a 3 mm wide thermal heating film.

The observable tunable response not only shows a shift in resonance behavior but also attenuation behavior. Around the same 2–4 GHz region, the change in S21 approximately -13 dB at the notch resonance, from -23 dB at 0 mA to -35 dB at 25 mA. This shows that the tunable response of the device produces not only tunable resonance shifts, but also tunable attenuation in transmission in this narrow band. From an application perspective, this behavior resembles more of a thermally tunable resonator or a frequency selective attenuator. Although this device is not optimized as a resonator or attenuator, the measured tunable response shows that the thermally controlled material has the capability to modulate the RF response for designs that have a specific application. The most interesting tunable response was in the transmission of the device, but the reflection parameters also show a similar trend at a smaller magnitude. Both S11 and S22 exhibit shifts in their resonant features past 2 GHz with increasing current. This supports that the induced heating of the sample directly impacts the CPW structure parameters rather random thermal variations.

These results demonstrate that the STO CPW device produces measurable RF tunability under electrical heating. Although the absolute performance is limited by design constraints, the bias-dependent shift verifies that the thermally controlled platform can significantly contribute to a tunable response of STO at radio frequencies. The result is most promising as a first demonstration of thermally tunable, frequency selective and attenuation behavior on STO, which can support future implementations using this material in the microwave region.

4.6 Summary

This chapter demonstrates the design, fabrication, and experimental measurements of the thermally controlled RF guided wave device on STO. The high permittivity of STO created major design challenges, leading to a practical CPW design near 25 Ω rather than an ideal 50 Ω line. Despite imperfections from impedance mismatch, material response, and PCB fixtures, the device produced a clear tunable shift in the measured S-parameters. This result shows that the Joule heating through the ITO layer directly provides significant tunability in the measured radio frequency region.

5 Conclusions & Future Work

5.1 Conclusions

This thesis investigated thermally tunable perovskite-oxide devices based primarily on strontium titanate across infrared, terahertz, and RF frequency regions. Thermal tunability was induced using electrically biased ITO thin films for localized Joule heating, allowing the electromagnetic response of STO samples and devices to be modified through controlled thermal biasing. I-V characterization, thermal imaging, and COMSOL simulations were used to characterize the heating behavior and establish the thermal platform used throughout these projects.

The strongest tunability was observed in the terahertz measurements. THz-TDS showed a clear tunable pulse delay and refractive index, and this demonstrated that STO under thermal change can strongly modify THz electromagnetic waves. The extracted extinction coefficient also showed that this sample has significant absorption loss, which must be considered in implementations at THz. The FTIR measurements showed a weaker but measurable tunable response, with the largest changes occurring near the larger wavelength and smaller frequency range. This contrast with the THz results is consistent with STO's stronger low-frequency dielectric response, where temperature sensitive polar phonon modes contribute more directly to the material's tunability at THz.

The RF guided-wave device demonstrated that thermal tuning can also be observed in a fabricated CPW structure on STO. Although the high permittivity of STO created impedance-matching challenges and forced a practical lower-impedance design, the measured S-parameters showed a clear bias-dependent shift in the transmission response near 2–4 GHz. These results show that thermally biased STO is a promising platform for tunable electromagnetic devices, especially

in the THz and RF regimes, while also highlighting important tradeoffs such as dielectric loss, impedance mismatch, and fabrication constraints.

5.2 Future Work

Future work should focus on moving the THz results from material based tunability toward application driven devices. The large shift in refractive index observed suggests that STO/ITO structures could be useful for tunable THz phase control, delay lines, or possible selective frequency components and devices. This would require optimizing the thermal biasing profile, reducing absorption loss possibly through thinner STO structures, and tailoring the STO/ITO geometry toward a specific THz function, such as phase control, tunable delay, or frequency-selective devices.

For the infrared measurements, future work could include a more complete optical characterization. The FTIR reflectance measurements showed measurable thermal response, but the apparent refractive-index calculation was limited because it does not fully account for STO absorption, which is important. Transmission measurements of the sample and modeling of the tunable response for the extraction of both refractive index and extinction coefficient would delve deeper into the infrared response and allow for more precise infrared characterization.

Lastly, for the RF device potential future work should focus on strongly redesigning the CPW geometry for better impedance matching, increased transmission across the RF path, and designing a device that operates effectively in a larger RF bandwidth. Designing with different sample sizes, substrate thicknesses, backside conductor geometries for larger heating area, and CPW dimensions should be investigated through more iterative simulation. Since the measured device already displays a significant tunable response, future RF designs could possibly target thermally tunable resonators, RF notch filters, or attenuators using STO/ITO as the base platform.

References

[1] A. Ahmed, I. A. Goldthorpe, and A. K. Khandani, "Electrically tunable materials for microwave applications," Applied Physics Reviews, vol. 2, no. 1, Art. no. 011302, 2015.

[2] A. Tombak, F. T. Ayguavives, J.-P. Maria, G. T. Stauf, A. I. Kingon, and A. Mortazawi, "Low voltage tunable barium strontium titanate thin film capacitors for RF and microwave applications," in IEEE MTT-S International Microwave Symposium Digest, 2000, pp. 1345–1348.

[3] H.-Y. Wu, C.-F. Hsieh, T.-T. Tang, R.-P. Pan, and C.-L. Pan, "Electrically tunable room-temperature 2π liquid crystal terahertz phase shifter," IEEE Photonics Technology Letters, vol. 18, no. 14, pp. 1488–1490, 2006.

[4] M. Kim, S.-H. Kim, C. Kang, S. Kim, and C.-S. Kee, "Highly efficient graphene terahertz modulator with tunable electromagnetically induced transparency-like transmission," Scientific Reports, vol. 13, Art. no. 6680, 2023.

[5] S. Wang, L. Kang, and D. H. Werner, "Active terahertz chiral metamaterials based on phase transition of vanadium dioxide (VO_2)," Scientific Reports, vol. 8, Art. no. 189, 2018.

[6] X. Chen et al., "Reconfigurable and nonvolatile terahertz metadevices based on a phase-change material," ACS Photonics, vol. 9, no. 5, pp. 1638–1646, 2022.

[7] L. Sponza, V. Véniard, F. Sottile, C. Giorgetti, and L. Reining, "Role of localized electrons in electron-hole interaction: The case of $SrTiO_3$," Phys. Rev. B, vol. 87, no. 23, Art. no. 235102, Jun. 2013, doi: 10.1103/PhysRevB.87.235102.

[8] C. Dupas et al., "High permittivity processed $SrTiO_3$ for metamaterials applications at terahertz frequencies," Sci. Rep., vol. 8, Art. no. 15275, Oct. 2018, doi: 10.1038/s41598-018-33251-y.

[9] Z. C. Zhao, M. Goryachev, J. Krupka, and M. E. Tobar, "Precision multi-mode dielectric characterization of a crystalline perovskite enables determination of the temperature-dependent phase transitions," IEEE Transactions on Ultrasonics, Ferroelectrics, and Frequency Control, vol. 69, no. 1, pp. 423–429, Jan. 2022, doi: 10.1109/TUFFC.2021.3108118.

[10] J. Han, F. Wan, Z. Zhu, and W. Zhang, "Dielectric response of soft mode in ferroelectric $SrTiO_3$," Applied Physics Letters, vol. 90, no. 3, Art. no. 031104, Jan. 2007, doi: 10.1063/1.2431448.

[11] T. Toyoda and M. Yabe, “The temperature dependence of the refractive indices of $SrTiO_3$ and TiO_2,” Journal of Physics D: Applied Physics, vol. 16, no. 5, pp. L97–L100, May 1983, doi: 10.1088/0022-3727/16/5/002.

[12] J. H. Haeni et al., “Room-temperature ferroelectricity in strained $SrTiO_3$,” Nature, vol. 430, no. 7001, pp. 758–761, Aug. 2004, doi: 10.1038/nature02773.

[13] C. G. Granqvist and A. Hultåker, “Transparent and conducting ITO films: New developments and applications,” Thin Solid Films, vol. 411, no. 1, pp. 1–5, May 2002.

[14] I. Hamberg and C. G. Granqvist, “Optical properties of transparent and heat-reflecting indium tin oxide films: Refinements of a model for ionized impurity scattering,” Journal of Applied Physics, vol. 59, no. 8, pp. 2950–2952, Apr. 1986.

[15] J. Txintxurreta et al., “Indium tin oxide thin film deposition by magnetron sputtering at room temperature for the manufacturing of efficient transparent heaters,” Coatings, vol. 11, no. 1, Art. no. 92, Jan. 2021.

[16] R. Usamentiaga, P. Venegas, J. Guerediaga, L. Vega, J. Molleda, and F. G. Bulnes, “Infrared thermography for temperature measurement and non-destructive testing,” Sensors, vol. 14, no. 7, pp. 12305–12348, 2014.

[17] H. B. Curtis, “Measurement of hemispherical total emittance and normal solar absorptance of selected materials in the temperature range 280° to 600° K,” NASA Lewis Research Center, Cleveland, OH, USA, NASA Tech. Rep., 1965.

[18] J. Neu and C. A. Schmuttenmaer, “Tutorial: An introduction to terahertz time domain spectroscopy (THz-TDS),” Journal of Applied Physics, vol. 124, no. 23, Art. no. 231101, Dec. 2018, doi: 10.1063/1.5047659.

[19] Menlo Systems GmbH, TERA K15 Time-Domain THz Spectrometer User Manual. Munich, Germany: Menlo Systems GmbH, 2018.

[20] J. M. Khosrofian and B. A. Garetz, “Measurement of a Gaussian laser beam diameter through the direct inversion of knife-edge data,” Applied Optics, vol. 22, no. 21, pp. 3406–3410, 1983.

[21] P. Dore, G. De Marzi, and A. Paolone, “Refractive indices of $SrTiO_3$ in the infrared region,” International Journal of Infrared and Millimeter Waves, vol. 18, no. 1, pp. 125–138, Jan. 1997.

[22] D. F. Santavicca, M. Colangelo, C. R. Eagle, M. P. Warusawithana, and K. K. Berggren, “50 Ohm transmission lines with extreme wavelength compression based on superconducting nanowires on high-permittivity substrates,” arXiv:2111.01006, Dec. 2021.

[23] S. Reza, “Coplanar Waveguide and Applications,” Sandia National Laboratories, Albuquerque, NM, USA, Rep. SAND2017-12410J, 2017.

[24] Z. Peterson, “SMA edge connector transitions in an RF PCB,” Altium Resources, May 10, 2023, updated Mar. 13, 2026. [Online]. Available: https://resources.altium.com/p/sma-edge-connector-transitions-rf-pcb. Accessed: Jul. 6, 2026.

[25] A. R. Djordjević, R. M. Biljić, V. D. Likar-Smiljanić, and T. K. Sarkar, “Wideband frequency-domain characterization of FR-4 and time-domain causality,” IEEE Transactions on Electromagnetic Compatibility, vol. 43, no. 4, pp. 662–667, Nov. 2001.